

Oxide nanowire arrays for light-emitting diodes and piezoelectric energy harvesters*

Sheng Xu[‡] and Zhong Lin Wang

School of Materials Science and Engineering, Georgia Institute of Technology, Atlanta, GA 30332, USA

Abstract: As an outstanding member in the oxide nanowire family, ZnO nanowire is widely studied for its optical, semiconductive, and piezoelectric properties. $\text{PbZr}_x\text{Ti}_{1-x}\text{O}_3$ (PZT), usually in the form of polycrystalline thin films, is known for its high piezoelectric coefficient and is an ideal material as actuator. In this review, we first briefly introduce the rational growth of ZnO and PZT nanowire arrays by seedless wet chemical methods. Utilizing the ordered ZnO nanowires grown on *p*-type substrates, we next present an array of single ZnO nanowire-based blue/near-UV light-emitting diodes (LEDs), including their fabrication process, electroluminescence (EL) spectra, and external quantum efficiency. Finally, we discuss the piezoelectric ZnO and PZT nanowire-enabled three-dimensionally integrated direct- and alternating-current nanogenerators, and their primary roles in self-powered nanosystems and for powering personal microelectronics.

Keywords: energy-harvesting devices; hydrothermal; nanowire arrays; optoelectronics.

INTRODUCTION

Nanomaterials and nanotechnology have shown tremendous potential to solve many problems facing energy needs nowadays [1]. In particular, oxide nanowires have received much attention for their unique structural and physical properties and are playing an important role in many energy studies, such as solar cells [2], water-splitting devices [3], Li-ion batteries [4], piezoelectric nanogenerators [5], supercapacitors [6], and optoelectronic devices for efficient energy usage [7]. In this review, we focus on two unique oxide nanowires: ZnO and $\text{PbZr}_x\text{Ti}_{1-x}\text{O}_3$ (PZT) nanowires. First, we demonstrate the versatile low-temperature wet chemical method to grow ZnO nanowire arrays and epitaxial single-crystalline PZT nanowire arrays. Second, we show the blue/near-UV light-emitting diodes (LEDs) composed of ordered ZnO nanowire arrays grown on *p*-GaN substrates. Third, based on the as-synthesized ZnO nanowire arrays, we demonstrate multilayered direct- and alternating-current nanogenerators. Self-powered solely ZnO nanowire-based nanosystems are presented by integrating a nanogenerator with a nanosensor together. Lastly, utilizing a full-wave bridge rectifier, we are able to rectify the alternating output of the PZT nanowire-based nanogenerator, and the rectified charges are accumulated to light up a laser diode (LD).

Pure Appl. Chem.* **83, 2115–2212 (2011). A collection of invited, peer-reviewed articles by the winners of the 2011 IUPAC Prize for Young Chemists.

[‡]Corresponding author: E-mail: shengxu@illinois.edu

RATIONAL GROWTH OF OXIDE NANOWIRE ARRAYS BY SEEDLESS WET CHEMICAL METHODS

Oxide nanowires can be synthesized by a wide range of approaches, among which the wet chemical methods are particularly attractive because of their low cost, environmental friendliness, and potential scale-up capabilities. The growth takes place at a relatively low temperature and is thus compatible with flexible organic substrates. It also does not require metal catalysts and thus can be integrated with the present Si technologies; besides, there are a variety of parameters that can be controlled to tune the density, morphology, and other properties of the nanowires reliably and reproducibly.

Density-controlled growth of high-aspect ZnO nanowire arrays on Au-coated smooth surfaces

ZnO nanowire is currently one of the most sought after research subjects in the entire field of physics [8], owing to its superior performance and wide applications [9,10]. Traditionally, ZnO nanowires were grown on seeded substrates, and the nanowire density was usually very high and could not be easily controlled [11,12]. In our study, by replacing the seeded substrate with a Au-coated one, fine density control of the ZnO nanowire arrays has been achieved on both Si wafers and flexible Kapton polymer substrates [13]. A 50-nm-thick layer of Au acts as a buffer layer to mitigate the large lattice mismatch between the substrate and the ZnO nanowire basal plane.



The growth nutrient solution was composed of a 1:1 mixture of zinc nitrate hexahydrate and hexamethylenetetramine (HMTA). Zinc nitrate provides Zn^{2+} ions required for building up ZnO nanowires. Water molecules in the solution provide O^{2-} ions. Although the exact function of HMTA during the ZnO nanowire growth is still under debate, it is believed to act as a weak base and gradually decomposes in water into ammonia and formaldehyde, to release the built-in strain energy of the molecule, as shown in eq. 1. The ammonia creates a basic environment, which facilitates zinc hydroxide formation, as shown in eqs. 2–4. At elevated temperatures, zinc hydroxide undergoes dehydration and produces ZnO. The slow decomposition of HMTA is critical because if the HMTA hydrolyzes very quickly, the Zn^{2+} ions in solution would precipitate very quickly owing to the high pH environment, which would result in fast consumption of the nutrients with minimal one-dimensional growth.

Shown on the left-hand side in Fig. 1 is an optical image of the experimental set-up. When heated in an oven, ZnO nanowires heterogeneously nucleate and grow on the substrate. It is worth noting that the substrate was floating facing down on the surface of the reaction solution by virtue of surface tension, which prevents the homogeneously formed ZnO nanostructures inside the bulk solution falling onto the substrate and inhibiting the regular growth of ZnO nanowires. The growth process of ZnO nanowires can be controlled through chemical reactions 1–5 as listed. All of the five reactions can be controlled by adjusting the reaction parameters, such as precursor concentration, growth temperature, and growth time, in order to push the reaction equilibrium forward or backward. In general, precursor concentration determines the nanowire density. Growth time and temperature control the ZnO nanowire morphology and aspect ratio.

The density of ZnO nanowires on the substrate could be controlled by the initial concentration of the zinc ions and HMTA. From 0.1 to 5 mM, the density of ZnO nanowires increased dramatically. This

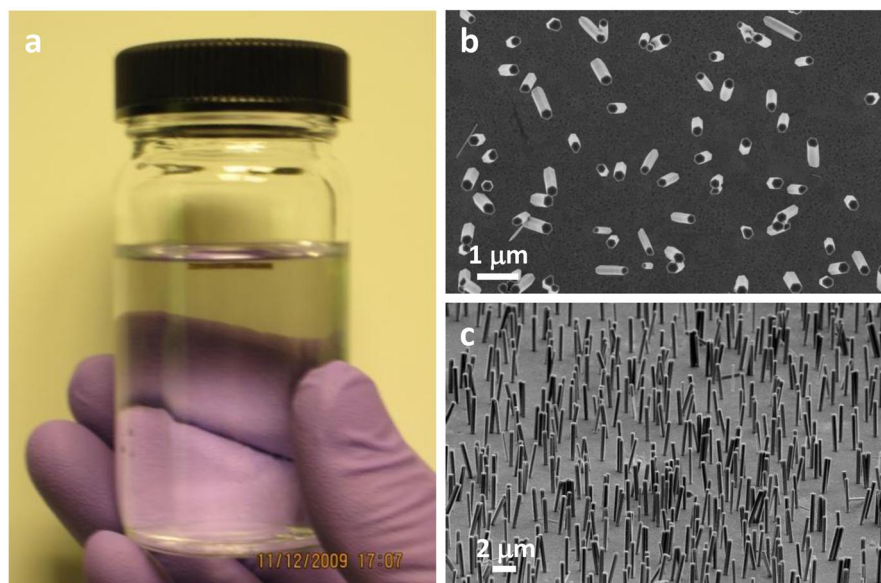


Fig. 1 (a) The camera image shows the actual reaction container before growth, where a substrate floating on the surface of the growth solution is clearly seen [14]. Scanning electron microscopy (SEM) images of (b) top view and (c) oblique view of the density-controlled ZnO nanowires on Au-coated general substrates [13].

can be attributed to the increase of the chemical potential of Zn^{2+} inside the bulk solution with its concentration, producing more nucleation sites on the substrate surface. When further increasing the zinc concentration, the density of ZnO nanowires remained approximately steady with a tendency to slightly decrease, while the surface coverage increases owing to lateral growth. The steady trend of the nanowire density may be understood from the nucleation and growth process. The nanowire density is decided by the number of nuclei formed at the initial stage of the growth. The arrival of more ions on the substrate may not initiate new nuclei at later stages; rather, they have higher probability to reach and attach to the existing nanowires rather than to the newly formed nuclei, and thus the size of the nuclei may not exceed the critical size and they will eventually dissolve into the bulk solution. This also explains why the grown nanowires have fairly uniform length.

Surfaces such as (0001) and (000 $\bar{1}$) in wurtzite ZnO are polar; growth on these surfaces results in axial growth of the nanowire; surfaces such as {01 $\bar{1}$ 0} and {2 $\bar{1}$ $\bar{1}$ 0} are nonpolar, and growth on these surfaces results in lateral growth. The growth rates of the polar and nonpolar surfaces were found to be different at various growth stages. In the initial stage (from the onset of reaction to ~30 min), both the width and length increased to about 300 nm. From 30 min to around 6 h, the width of ZnO nanowires was almost independent of time, while the length increased to about 2 μm . From 6 to 48 h in the study, the size of ZnO nanowires almost doubled, keeping the aspect ratio nearly unchanged. Therefore, in the beginning, lateral growth was as significant as axial growth; in the following stage, axial growth was dominant; and at the final growth stage, lateral growth and axial growth seemed to be equally significant.

Temperature is an important factor in controlling the aspect ratio and the shape of ZnO nanowires. At a lower reaction temperature, the aspect ratio became small, which indicates that the polar surface has a relatively lower growth rate than nonpolar surfaces at low temperatures. At a higher reaction temperature, on the other hand, the shape of the nanostructure grown became pyramidal. The shape change can be explained by the shift of chemical equilibrium in the reactions involved. In reaction 1, 7 mol of reactant produced 10 mol of product. With increased temperatures, reaction 1 would move forward by

virtue of entropy increase, resulting in higher decomposition rate of HMTA. Therefore, at the initial stage of reaction, HMTA has already decomposed to a relatively large degree and produced sufficient OH^- for ZnO growth, so the base of ZnO nanorods is thicker than at lower temperatures. As the supply of Zn^{2+} gradually becomes exhausted, the diameter of the nanowire would gradually decrease, forming a pyramidal shape.

The ZnO nanowires synthesized via this method are of low aspect ratios, typically 10 to 15 [12], which greatly limits their applications where flexible or high surface-to-volume ratio nanowires are needed. To increase the aspect ratio, capping agents such as ethylenediamine [16] and polyethylenimine [2] can be added. However, these capping agents might also introduce certain impurities into the ZnO nanowires, undermining their properties and performance. Without capping agents, improvement of the aspect ratio proved to be challenging, because reaction parameters such as precursor concentration, growth time, and growth temperature worked together in a convoluted manner toward the final growth product. Most reported studies employed inefficient cook-and-look methods, and lacked theoretical guidance in experimental design.

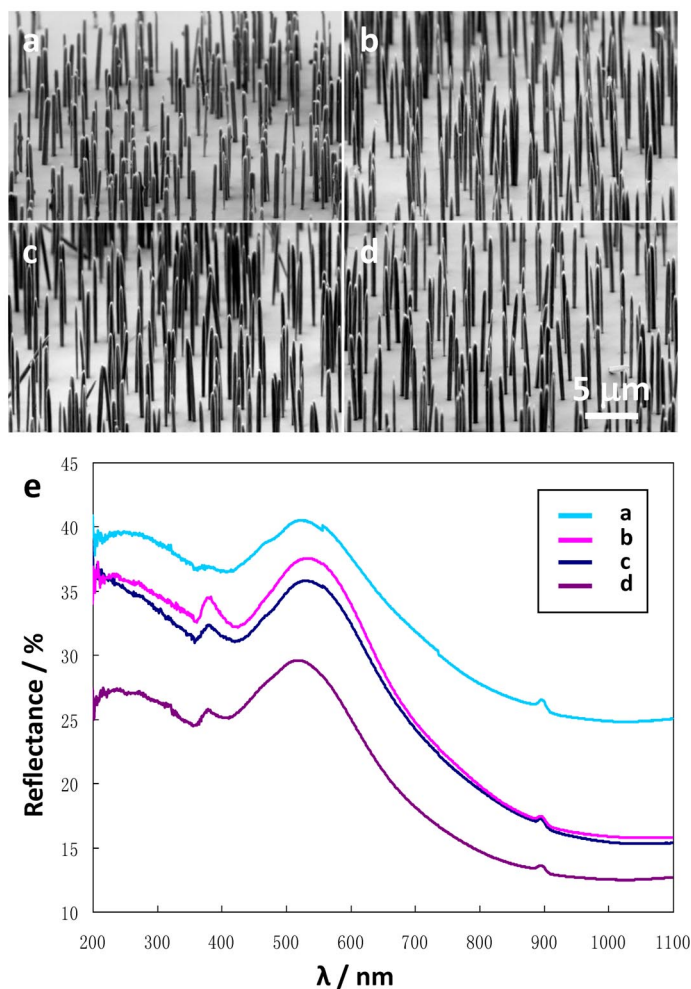


Fig. 2 SEM images of ZnO nanowire arrays with an aspect ratio of (a) 15.1, (b) 20.1, (c) 20.9, and (d) 22.3, respectively, and (e) their corresponding reflectance spectra [15].

By utilizing a statistical design and analysis method, a systematic approach to optimize the aspect ratio of hydrothermally grown ZnO nanowire arrays was developed in our study [15]. The statistical design and analysis methods were very effective in reducing the number of experiments performed and in identifying the optimal experimental parameters, and also enabled the experimentalists to change more than one parameter at a time and analyze the relationship between the different reaction parameters. In this study, classic statistical analysis was inapplicable owing to the uncontrollable variation in the process and complex interactions among various factors. Instead, pick-the-winner rule [17] and one-pair-at-a-time main effect analysis [18] were used to identify optimal reaction settings. By controlling the hydrothermal reaction parameters (precursor concentration, growth time and temperature, and possibly capping agent), the aspect ratio of ZnO nanowires was improved from around 10 to nearly 23 without capping agent addition (Figs. 2a–d).

The high aspect ratio nanowire arrays were found to exhibit enhanced antireflection properties. As illustrated in Fig. 2e, curves A, B, C, and D correspond to ZnO nanowires of aspect ratio of 15.1, 20.1, 20.9, and 22.3, respectively. These four nanowire arrays have approximately the same nanowire density, as shown in their scanning electron microscopy (SEM) images. Obviously, at an incident angle of 60°, the ZnO nanowire arrays with an aspect ratio of 22.3 have 30 % stronger capability to suppress the reflection than those with an aspect ratio of 15.1 in both the UV and visible range. That is simply because longer nanowires would have a much higher chance to interact with the photons on their surfaces than shorter ones, and therefore the absorption cross-section would be considerably larger, leading to a broadband suppression in reflection.

Patterned growth of ZnO nanowire arrays on inorganic substrates at low temperature without catalyst

To grow high-quality ZnO nanowire arrays for sensor arrays, piezoelectric antenna arrays, LEDs, and waveguides, it is necessary to meet the following three requirements. First, the growth has to be at low temperature so that it can be integrated with general substrates. Second, the nanowires have to be grown following a designed pattern, with a high degree of control in size, orientation, dimensionality, uniformity, and possibly shape. Finally, the catalyst should be eliminated for integration with Si-based technology. Combined with electron beam lithography (EBL), the hydrothermal process can satisfy all of these requirements.

The growth scheme is illustrated in Fig. 3. Wurtzite-structured ZnO nanowires have intrinsic polar surfaces terminated with Zn^{2+} plane and O^{2-} plane, respectively. These surfaces have higher surface energy and more active sites, to which the newly arrived precursor molecules are more likely to adsorb, resulting in fast growth along $\langle 0001 \rangle$. From a crystal structure point of view, wurtzite-structured ZnO nanowires have a six-fold symmetry at the basal plane and a two-fold symmetry at the side surfaces, as illustrated in Fig. 3 in different colors. On a six-fold symmetry epitaxial substrate, such as $\text{GaN}\{0001\}$ and $\text{ZnO}\{0001\}$, ZnO nanowires would grow vertically on the substrate. On a two-fold symmetry substrate, such as $\text{ZnO}\{01\bar{1}0\}$ and $\text{ZnO}\{2\bar{1}\bar{1}0\}$, ZnO nanowires would grow horizontally on the substrate. To control the growth patterns, a thin layer of e-beam resist [typically, polymethyl methacrylate (PMMA)] was first spin-coated on the substrate, then patterned by EBL, and finally developed. The e-beam resist that was exposed to the electron beam was washed away, exposing the substrate underneath on which ZnO nanowires nucleated.

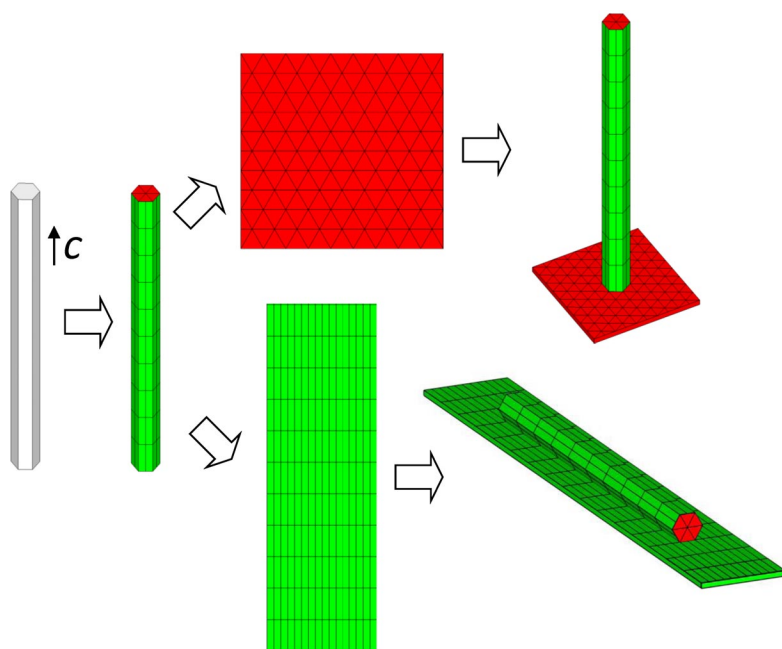


Fig. 3 Illustration of epitaxial growth strategy for vertical and horizontal ZnO nanowire arrays, respectively [14].

Vertically aligned ZnO nanowires have a variety of applications in electronics, optoelectronic and electromechanical nanodevices. For GaN(0001) substrate, the lattice mismatch between GaN{0001} and ZnO{0001} planes is 1.8 %, which led to a perfectly aligned growth of ZnO nanowire array, as shown in Figs. 4a,b. To prevent collapsing of the vertical nanowires owing to surface tension when drying, the sample requires supercritical drying after the hydrothermal growth is complete [19]. The vertical alignment of the as-grown ZnO nanowire arrays was examined by X-ray diffraction rocking curve measurements, and the rocking curve for the peak at 34.393° of the ZnO (0002) plane exhibited a full width at half maximum (FWHM) value of 0.15° , which indicated almost perfect vertical alignment.

An interesting phenomenon was noticed when the EBL pattern before hydrothermal growth was compared with that after growth. Out of 100-nm-sized holes, the as-grown nanowires were approximately 300 nm in diameter. A two-step growth model for the ZnO nanowires was proposed. In the first step, the nanowire grew out of the e-beam-resist hole with the same lateral dimension as confined by the hole. After that, there was no lateral confinement, and the nanowire could grow both vertically and laterally, but apparently faster in vertical direction than in lateral direction owing to its anisotropy. The nanowire dimension is determined by the physical confinement from the e-beam resist as well as the growth parameters, such as the precursor concentration, temperature, and time. In general, low precursor concentration, high growth temperature, and moderate growth time favor thin and high-aspect-ratio nanowires; high precursor concentration, low growth temperature, and too long or too short growth time tend to produce thick and low-aspect-ratio nanowires [13]. Other than that, the width of the nanowires could also be effectively and efficiently controlled by defining different sizes of the e-beam-resist openings [20,21]. The patterned growth could be easily scaled up with JEOL JBX-9300FS EBL system. As shown in Figs. 4c,d, a $200 \times 200\text{-}\mu\text{m}$ -sized ZnO nanowire array, with 100 nm in opening diameter and $1\ \mu\text{m}$ in pitch, could be finished within less than 2 min.

On the other hand, horizontal ZnO nanowire arrays have as many potential applications as the vertical ones. Owing to unresolved technical issues, there has been very little progress in this area though. Several methods had been reported, such as growing ZnO nanowires out of pre-patterned side walls of

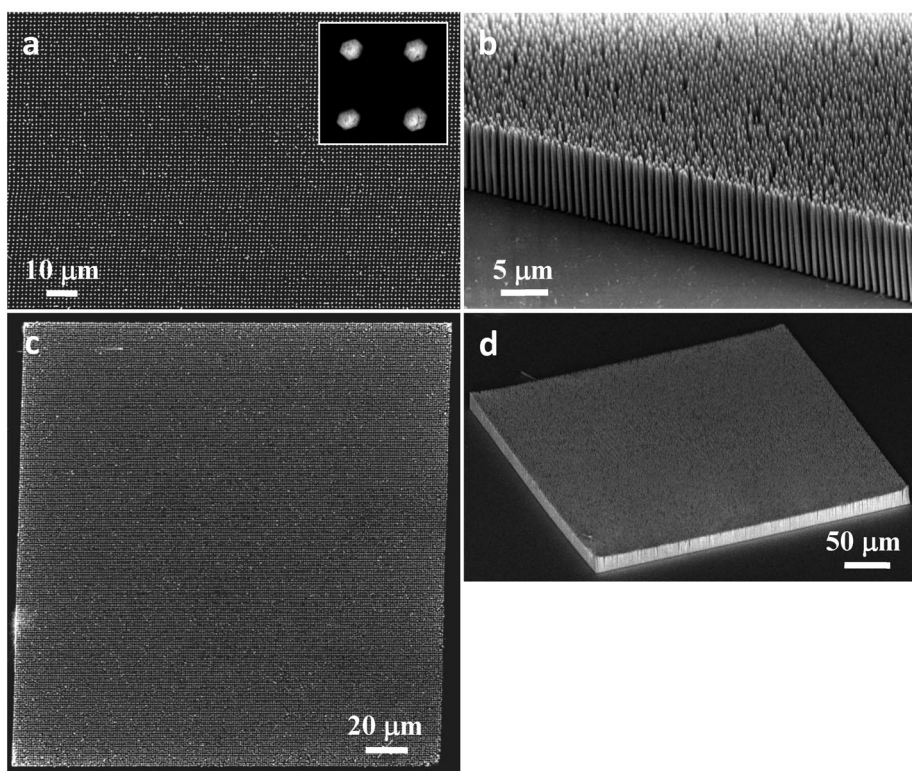


Fig. 4 (a) Top view and (b) 60° tilt view of the ZnO nanowire arrays on a GaN substrate. Inset in (a) is enlarged image showing the in-plane alignment of the nanowires. (c) Top view and (d) 60° tilt view of a 200 × 200 μm patterned nanowire array with 1 μm in pitch [20].

a thin ZnO seed layer, or metal-catalyzed growth on planar alumina substrate by hydrothermal decomposition [22], physical vapor deposition (PVD) [23], or metal-organic chemical vapor deposition (MOCVD) [24]. But the resulting nanowires were rather sparse and random in horizontal orientation, or of poor horizontal alignment. Post-growth horizontal alignment was achieved by dispersing the nanowires into solvents under a high-frequency alternative electrical field but with random crystallographic orientation [25].

By using a variation of the patterned vertical nanowire growth technique, horizontal ZnO nanowire arrays were fabricated with superior control over their dimensionality, orientation, and uniformity, as shown in Fig. 5a. To grow the patterned horizontal nanowires, single-crystal A-plane ZnO {2 $\bar{1}\bar{1}$ 0} substrate with e-beam resist was patterned by arrays of physical lines and rectangles with different lengths and widths. The resist opening should be oriented parallel to the <0001> direction of the substrate in order to achieve uniform nanowire morphology since the single-crystalline substrate has the *c*-axis lying parallel to the top surface plane. Hydrothermal growth was conducted by a similar approach as described previously. After growth, the substrate was cooled down to ambient temperature and then was immersed in IPA to remove the absorbed water.

Size expansion was also observed here as in the vertical case, and the lateral overgrowth could be utilized to grow novel multi-segment nanowire superstructures, as shown in Fig. 5b. To make the superstructures, an array of e-beam-resist openings with different widths was defined to be separated from each other. When the nanowires grow out of the e-beam-resist openings, they tend to expand and eventually merge with each other, forming these continuous multi-segment superstructures. Each and every individual segment has an epitaxial relationship with the single-crystalline substrate, so the as-grown

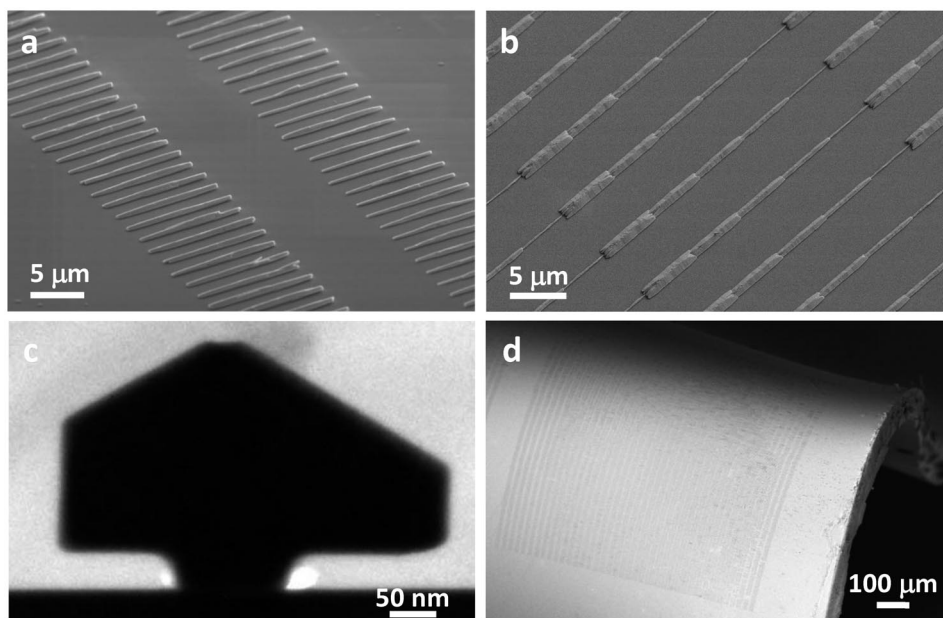


Fig. 5 SEM images of (a) horizontal ZnO nanowires arrays [21], and (b) a horizontal ZnO nanowire array-based five-segment monolithic superstructure [26]. (c) TEM cross-section view of the horizontal ZnO nanowires with the substrate [26]. (d) Low-magnification SEM images of the two-segment nanowire arrays after transferring on a flexible substrate [26].

continuous superstructures are considered to be monolithic single crystals. Using this methodology, we could fabricate an array of ultra-long ZnO nanowires with lengths on the order of millimeters and widths on the order of hundreds of nanometers, achieving an aspect ratio on the order of 10000. Compared with making an array of continuous ultra-long e-beam-resist openings, this method is more time-efficient.

Figure 5c shows a cross-section of the horizontal nanowires in transmission electron microscopy (TEM). E-beam resist on the substrate has been removed by annealing at 500 °C for 30 min, which also helps improve the crystallinity of the nanowires. The cross-section of the nanowire appears like a mushroom with the root about 100 nm wide, as defined by the size of the e-beam-resist opening. The nanowire expands laterally, forming two wings after growing out of the e-beam-resist opening. The separation between the wings and substrate surface is about 50 nm, which is the thickness of the e-beam resist. High-resolution TEM (HRTEM) studies have indicated that on the $(2\bar{1}\bar{1}0)$ surface of the substrate, the as-grown nanowire is enclosed by well-defined $(01\bar{1}0)$ facets with a surface roughness of less than 2 nm. Selected area electron diffraction patterns from the single nanowire confirm its growth orientation along the c -axis; patterns from the substrate confirm the orientation of the substrate; and patterns from the two together prove their epitaxial orientation relationship.

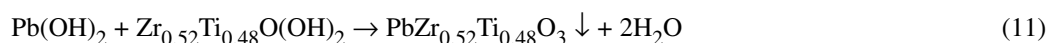
The single-crystalline ZnO substrate is mechanically rigid and brittle, which limits their application in flexible electronics, and ZnO is also electrically conductive, which does not allow direct device fabrication on the substrate. In our study, an effective way was demonstrated to lift off these horizontal nanowires and transfer them onto a mechanically flexible and electrically insulating polymer substrate, which greatly expands their potential applications [26]. To do so, the nanowire arrays were first encapsulated with PMMA prepolymer, which was later cured and bonded to the existing PMMA. The cured PMMA thin film was delaminated, and in the process the horizontal nanowire arrays were lifted off and transferred onto flexible PMMA thin film. Oxygen plasma was optionally applied to etch a thin top sur-

face layer of the PMMA film and partially expose the buried nanowire arrays. Photodetectors were fabricated based on the as-transferred nanowire arrays, and showed good response to UV light.

Hydrothermal epitaxial growth of PZT nanowire arrays

Lead zirconate titanate, PZT, is one of the most important piezoelectric materials for sensors and actuators, owing to its outstanding piezoelectric performance [27,28]. However, the fabrication of PZT thin films [29] and microfibers [30] usually requires high temperatures (~650 °C) to increase the crystallinity [31], which leads not only to high cost and incompatibility with general fabrication processes but also makes it difficult to integrate with soft materials, even though a transfer technique has been demonstrated recently [32]. The first chemical epitaxial growth of vertically aligned single-crystal $\text{PbZr}_{0.52}\text{Ti}_{0.48}\text{O}_3$ nanowire arrays has been demonstrated on a variety of conductive and non-conductive substrates by hydrothermal decomposition at 230 °C, overcoming the above-stated drawbacks.

The proposed reaction equations are listed below. The vertical growth and alignment were enforced by the epitaxial growth on the substrates, such as 0.7 wt % Nb-doped SrTiO_3 (STO) (100) and 0.01 wt % Fe-doped STO (100) (~0.007 $\Omega\cdot\text{cm}$). The hydrothermal decomposition temperature plays an important role in the growth of $\text{PbZr}_{0.52}\text{Ti}_{0.48}\text{O}_3$ nanostructures. As shown in Figs. 6a–c, from 170 to 230 °C, the structures change gradually from thin film to nanowire, which is probably due to more oriented growth behavior at high reaction temperatures. From Figs. 6a,b, the nanostructures show perfect vertical and in-plane alignment. For the nanowires, they are less straight and vertically aligned as in the case of ZnO nanowires (Fig. 4b), probably due to the low Young's modulus of PZT (86 GPa) compared with that of ZnO (127 GPa). Energy-dispersive spectrum (EDS) in Fig. 6d confirms the elements present in the PZT nanowires. The poly(vinyl alcohol) and poly(acrylic acid) were believed to perform as capping agents chemisorbing at the side surfaces of the nanowires, as can be clearly seen as an amorphous layer in Fig. 6e, and thus inhibiting the nanowire from radial growth. HRTEM analysis of a single nanowire (Fig. 6e) and X-ray diffraction of a nanowire array (Fig. 6f) show that the as-synthesized nanowires have a tetragonal phase (space group P4mm) with a [001] growth direction [33]. A piezoelectric domain boundary was found in the axial direction of the nanowire, but the entire nanowire preserves a single-crystal structure.



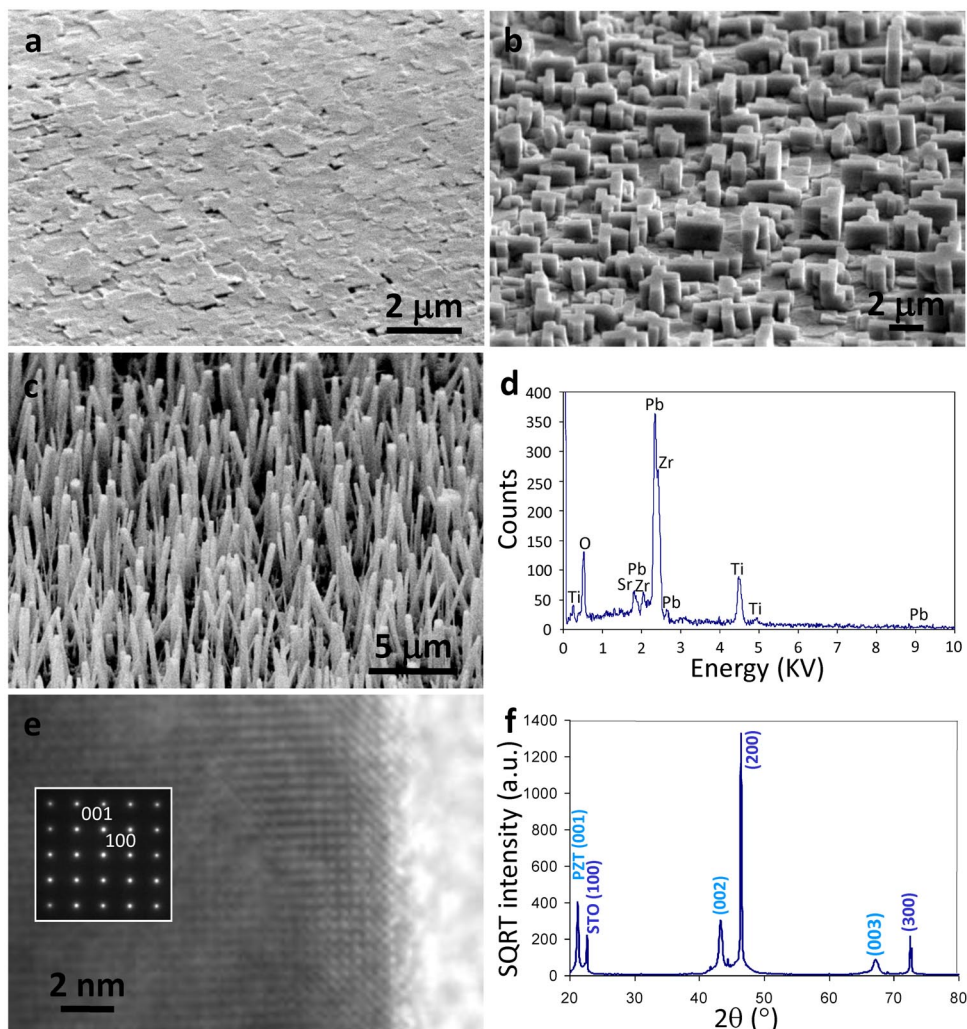


Fig. 6 (a–c) SEM images showing the structural evolution of the epitaxially grown $\text{PbZr}_{0.52}\text{Ti}_{0.48}\text{O}_3$ nanostructures as a function of growth temperature. (d) EDS acquired from the PZT nanowire showing its chemical composition. (e) HRTEM image and electron diffraction pattern (inset), indicating a well-crystallized tetragonal phase with a lattice constant of $a = 3.93 \text{ \AA}$ and $c = 4.16 \text{ \AA}$. (f) Conventional θ - 2θ scan X-ray diffraction (XRD) [34].

ORDERED ZINC OXIDE NANOWIRE ARRAY AS BLUE/NEAR-UV LED

ZnO-based LEDs are considered as a potential candidate for the next generation of blue/near-UV light sources [35], owing to their direct wide bandgap energy of 3.37 eV, a large exciton binding energy of 60 meV at room temperature, and several other manufacturing advantages of ZnO [36], including the availability of large area substrates at a relatively low cost, amenability to wet chemical etching, great tolerance to high-energy radiation, and long-term stability. Based on the patterned vertical ZnO nanowire arrays as shown previously [20], blue/near-UV LEDs composed of arrays of n -ZnO nanowires on a p -GaN thin film substrate were demonstrated with a capability of controlling the spatial distribution [37].

Fabrication of the heterostructural LED

While the pursuit of stable and reproducible p -ZnO is still ongoing [38], heterojunctions of n -ZnO and p -GaN were employed as an alternative approach considering the similar crystallographic and electronic properties of ZnO and GaN. The design of the LED is shown in Fig. 7a. Ordered ZnO nanowire arrays were first grown on p -GaN [13,20]. Ohmic contact to the bottom p -GaN was made by depositing 30 nm/30 nm layers of Ni/Au on the p -GaN followed by rapid thermal annealing in air at 500 °C for 5 min, as was confirmed by the individual I - V curves, and the rectifying I - V curve comes only from the p - n diode herein. A 50-nm conformal layer of SiO₂ was deposited onto the nanowire arrays by plasma-enhanced chemical vapor deposition. Then a relatively thick layer of PMMA was spin-coated onto the substrate to wrap around the nanowires. During this process, the SiO₂ layer protected the nanowires from falling down owing to the surface tension of the PMMA. Then oxygen plasma was applied to etch away the top part of the PMMA followed by reactive ion etching (RIE) to remove the top SiO₂, exposing the tips of the nanowires. Since the oxygen plasma and RIE were only applied to the tip part of the nanowires, possible deterioration they might have induced to the electrical and optical properties of the nanowires could be neglected. Finally, a 100-nm layer of indium tin oxide (ITO) was sputtered as the top common electrode of nanowires.

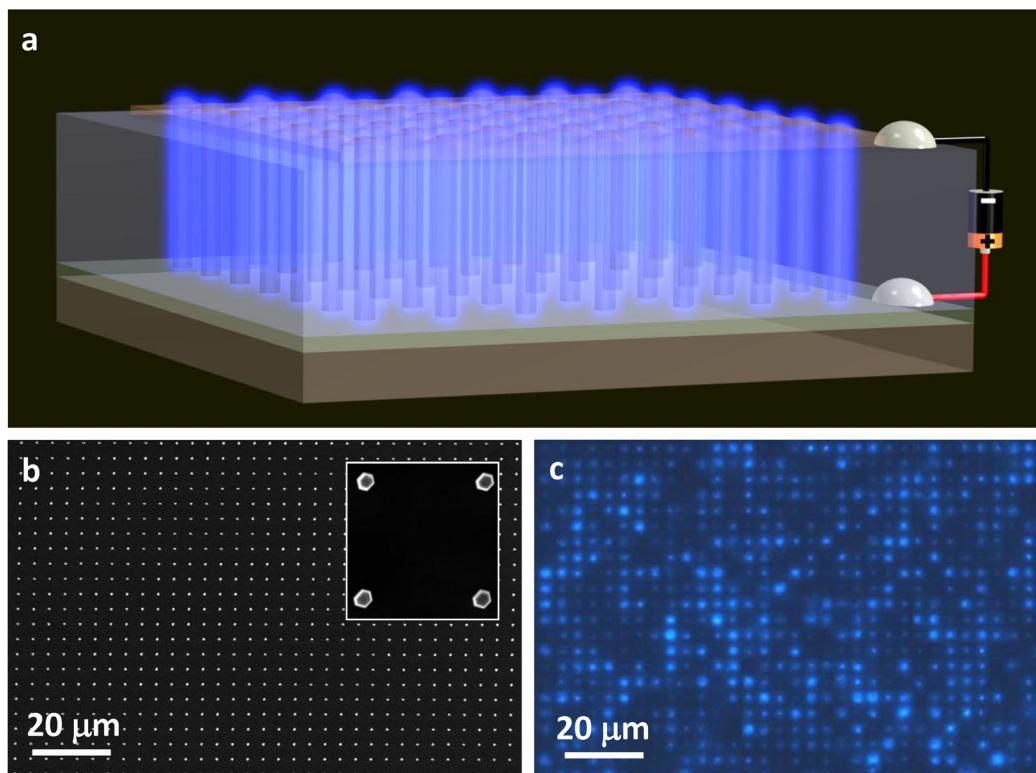


Fig. 7 (a) Schematic representation of the structure overview of the LED. (b) Top view of the as-grown patterned vertical ZnO nanowires, and (c) optical image of a working LED at a bias voltage of 10 V (artificial bluish color) [37].

Electroluminescence spectra and characteristics of the emission peaks

The optical image of a working blue/near-UV light was recorded under Nikon Eclipse Ti inverted fluorescence microscope with 9 s exposure time and a gain value of 1, as shown in Fig. 7c. In the device, all of the nanowires are connected in parallel and each single nanowire is a light emitter. The brightness difference among the individual nanowires probably comes from the current crowding effect and different serial contact resistances, therefore, different injection currents through the individual nanowire. The pitch between each lighting spot shown in Fig. 7c is 4 μm , and the resolution is 6350 dpi.

The physical origin of this electroluminescence (EL) has been extensively studied but is still under debate [39,40]. As shown in Fig. 8a, emission spectrum of the as-fabricated LED was monitored at different bias voltages/injection-currents at room temperature. From 4 to 10 V, the contour of the EL spectrum does not change much with the bias voltage. The dominant emission peak is slightly blue-shifted in the range of 400–420 nm with an FWHM of about 60 nm. The peak intensity vs. injection current ($L - I^m$) characteristics have been acquired, showing a superlinear relationship with $m = 1.3$. Peak-deconvolution with Gaussian functions [40,41], inset in Fig. 8a, shows that the broad spectrum consists of three distinct bands (Fig. 8b) centered in the range of 395–415, 420–440, and 450–510 nm, respectively, and each emission band corresponds to a particular recombination process. The near-UV emission band centered at around 400 nm is attributed to the near-band-edge (NBE) emission in ZnO nanowires that originates from the recombination of ZnO-free and -bound excitons [42,43]. Whereas the red-shifted violet emission band centered at about 430 nm is ascribed to the transitions from the conduction band or shallow donors to deep Mg acceptor levels in the *p*-GaN thin film substrate [36,42,43]. The blue emission around 460 nm comes from the radiative interfacial recombination of the electrons from *n*-ZnO and holes from *p*-GaN [42,44,45].

There has been a controversy about whether the emission is from the *n*-ZnO side [46,47] or the *p*-GaN side [36,43]. In this context, both scenarios had contributions. The hole concentration in the Mg-doped *p*-GaN substrate ($p \sim 10^{18} \text{ cm}^{-3}$) is higher than the electron concentration in the *n*-ZnO nanowire ($n \sim 10^{17} \text{ cm}^{-3}$), but the carrier mobility in the *p*-GaN is smaller than that in the *n*-ZnO. The barrier heights at the interface for the holes (0.57 eV) and for the electrons (0.59 eV) are similar. Therefore, the charge injection by electrons and holes from both sides should be comparable. Of course, the energy band offset at the ZnO/GaN interface is likely to be determined by the fabrication process [48]. The interface states generally act as nonradiative centers that annihilate free electrons and holes. Therefore, it is required to get a high-quality interface between the heterojunctions in order to get high-efficiency LEDs. The weak red emission at around 790 nm is coming from the native deep-level point defects (oxygen vacancies and zinc interstitials) in ZnO nanowires [43].

As the bias voltage is increased, the intensity of the main peak and all of the four sub-bands (including the defect emission) exponentially increases and also blue-shifts (Fig. 8b). The blue shift has been explained to be caused by several different mechanisms, such as band renormalization and band filling [49], and the screening effect of the built-in piezoelectric field [50]. Here, the blue shift of the emission peak comes from two resources: the blue shift of sub-band positions (Fig. 9a), and the change of relative intensities of the sub-bands at different injection currents (Fig. 9b) [42]. The blue shift of the ZnO and GaN NBE emission positions (Fig. 9a, i and ii) may be caused by the recombination of electrons and holes with higher kinetic energies at higher bias voltages, which could contribute to the energy of the emitted photons, assuming carrier mobilities remain nearly constant at moderate bias voltages. The most obvious blue shift of the peak position comes from the interfacial recombination process (Fig. 9a, iii), which could be understood from the band diagram. As the bias voltage is increased, the gap between the two quasi-Fermi levels is increased, and the interfacial recombination energy of the electrons from the ZnO side and holes from the GaN side goes up.

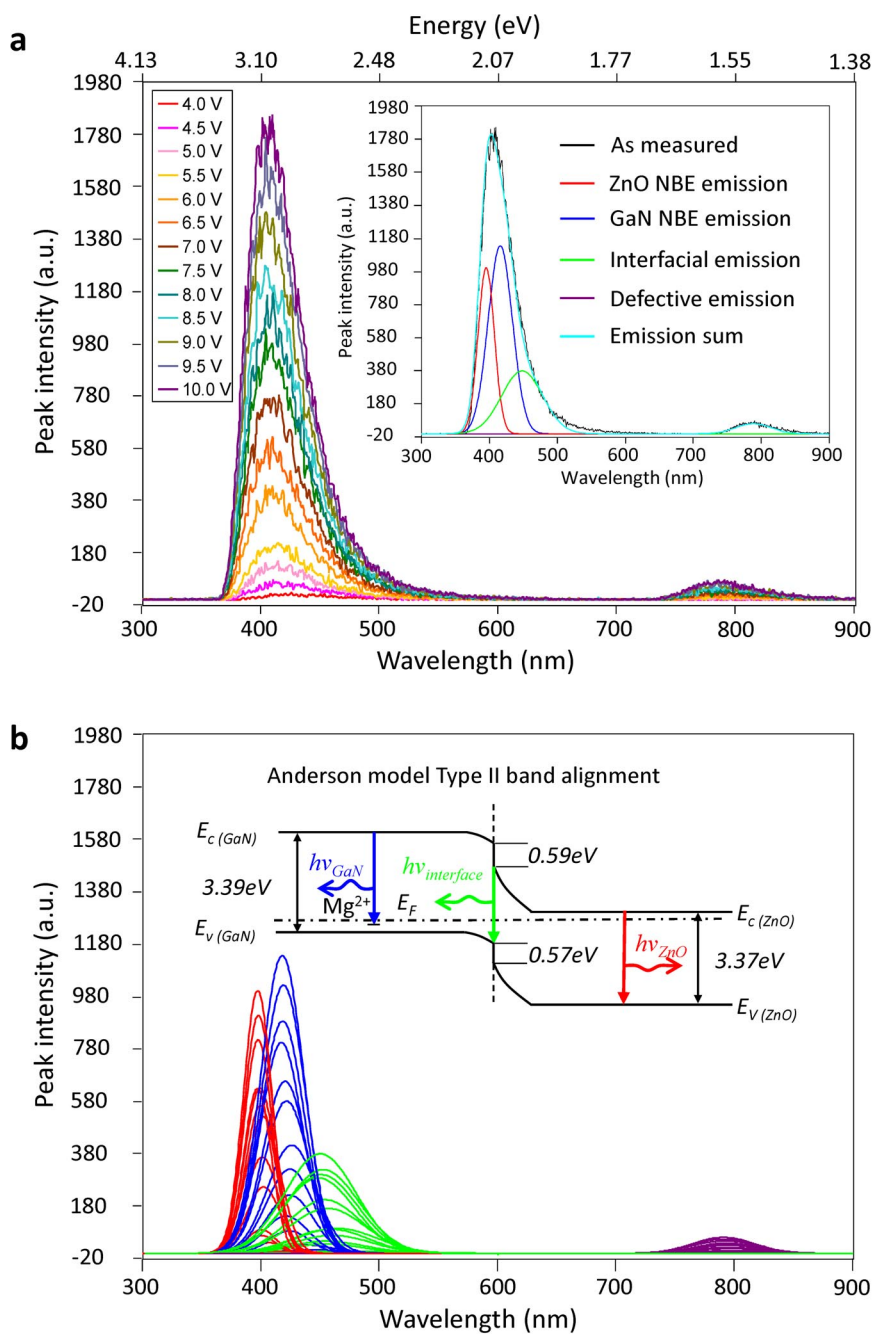


Fig. 8 (a) EL spectrum as a function of the forward bias voltage. Inset shows by Gaussian deconvolution analysis the blue/near-UV emission could be decomposed into three distinct bands that correspond to three different optoelectronic processes. (b) All of the four emission bands evolve (band width, height, and intensity) as a function of the bias voltage. Inset schematics show the band diagram of the *n*-ZnO/*p*-GaN heterojunction under no or small bias voltage, where the three emission bands comprising the blue/near-UV light are specifically indicated in different colors [37].

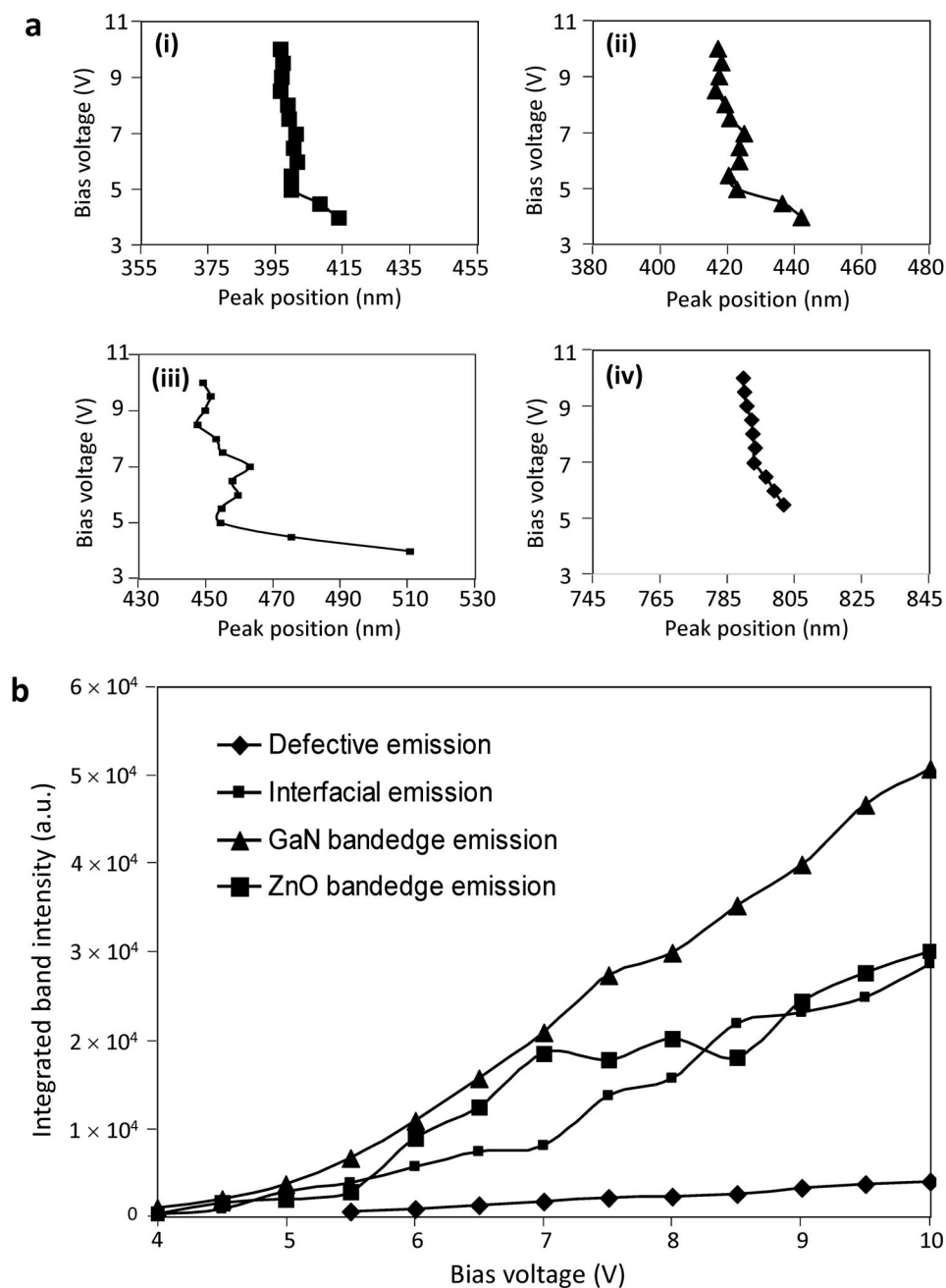


Fig. 9 (a) Peak positions blue-shift as a function of the bias voltage for (i) ZnO NBE emission, (ii) GaN NBE emission, (iii) interfacial emission, and (iv) defective emission. (b) The integrated emission bands intensity as a function of the bias voltage. For the defective emission, when the bias voltage is below 5.5 V, it is hardly distinguished from the noise level [37].

The blue shift of the EL spectrum also comes from the change of the relative intensity of the three bands, as shown in Fig. 9b. The intensity of the GaN NBE emission increases faster with bias voltage than the ZnO NBE emission and the interfacial emission. As the bias voltage is increased, the band bending of the *p*-GaN and *n*-ZnO is reduced, therefore, the electrons and holes have higher kinetic energies and much higher probability to cross the interfacial barrier and recombine at the other side. Moreover, comparison of the curve for ZnO NBE emission and that for GaN NBE emission yields interesting information (Fig. 9b). At low bias voltages (<7.0 V), both intensities are comparable; at high bias voltages (>7.0 V), the intensity of ZnO NBE emission is lower than that of GaN. In comparison with the high-quality GaN thin film fabricated by MOCVD, the relatively high level of native defects in the hydrothermally grown ZnO nanowires could undermine its internal quantum efficiency. These point defects in the ZnO nanowires perform like trapping centers and give rise to nonradiative recombinations.

External quantum efficiency of the heterostructural LED

Flat thin-film-based LEDs are suffering from the intrinsic drawback of low light extraction efficiency as limited by total internal reflection. Extensive research efforts have been made to address this issue, such as roughening the surface of the emitting thin film [51], reshaping the geometry of the LED architecture [52], utilizing resonant cavity [53], coupling with surface plasmon [54], and fabricating photonic crystal structures [55], etc. Among these approaches, nanowire/thin film heterostructures have been proposed to be a promising method owing to the waveguiding properties of nanowires [56–61].

Under the single-mode waveguide cavity condition [58], the single-mode cut-off value:

$$V = 2\pi \frac{a}{\lambda_0} \left(n_1^2 - n_2^2 \right)^{\frac{1}{2}} = 2.405, \text{ where } a \text{ is the diameter of the nanowire, } \lambda_0 \text{ is the free space wavelength}$$

of the propagating light (here we set it to be 400 nm), and n_1 (2.10) and n_2 (1.59) are the effective refractive index of the ZnO nanowire and the cladding PMMA thin film, respectively. In this case, 86.5 % of the light would be confined within a 223-nm-thick nanowire. Note that the facets of the nanowire are assumed to be perfectly flat in the single-mode condition calculations. In reality, however, these nanowires have rounded tips and a large surface-to-volume ratio, and thus a high density of surface states near the band edge, which results in considerable reduction of the back reflections at the ZnO nanowire surfaces. The phenomenon is known as the omnidirectional reflector effect [62]. Besides, based on an effective medium theory, these graded refractive indices of GaN (2.49), ZnO (2.10), and PMMA (1.59) could largely reduce the Fresnel reflection between GaN/ZnO and ZnO/PMMA interfaces, which facilitates optical transmission.

By virtue of these advantages, light could easily be extracted through multiple scattering in the nanowire structure. ZnO has a transmittance of over 90 % in the visible range [57], so the self-absorption of the nanowires should not be a major concern. To take one step further, the ZnO nanowire arrays were patterned to form a two-dimensional photonic crystal, which has an optical bandgap for the light travelling parallel to the surface of the substrate. By controlling the periodicity of the nanowire arrays, it is possible to match the wavelength of the emitted light to the bandgap of the photonic crystal, resulting in normal directional emission of the light.

The external quantum efficiency was calculated by acquiring the ratio of the output optical power and the input electrical power. The external quantum efficiency of the LED is about 2.5 %, which is considerably high for a single *p-n* junction-based LED, and such data are reproducible and consistent for different devices. As the bias voltage/injection current is gradually increased, the external quantum efficiency becomes steady, which indicates that the serial resistance and the nonradiative recombination through the defects, e.g., Auger recombination, do not increase in proportion with increasing the injection current.

THREE-DIMENSIONAL NANOGENERATORS WITH HIGH POWER OUTPUT

The search for sustainable micro-/nanopower sources for driving wireless and mobile electronics is an emerging field in today's energy research, which could offer a novel solution to the energy need of nanodevices/nanosystems [63–65]. The piezoelectric nanogenerator that converts the kinetic energy of low-intensity environmental vibrations into electricity was first demonstrated using ZnO nanowire arrays [5]. Following this initial discovery, both direct- [66–68] and alternating-current [69] nanogenerators have been developed. Nanogenerators based on other materials, such as GaN nanowires [70–72], InN nanowires [73], AlGaIn nanocones [74], CdS nanowires [75], ZnO/ZnS heterojunction nanowires [76], PZT nanofibers [30], nanoribbons [32,77–80], nanotubes [81], and single-crystalline nanowires [34], BaTiO₃ nanowires [82], NaNbO₃ nanowires [83], and poly(vinylidene fluoride) (PVDF) nanofibers [84,85], have shown promising potential for enhancing the nanogenerator performance. Consequently, a worldwide effort has been launched in this area, forming a new research field in nanotechnology and energy science [86]. The advantage of using nanowires for energy harvesting lies in their high piezoelectric coefficient, high elasticity, resistance to fatigue, and responsiveness to tiny random mechanical disturbances.

Multilayered direct-current nanogenerator fabricated by using paired ZnO nanotip-to-nanowire brushes

The previously developed direct-current nanogenerator was based on a vertically aligned ZnO nanowire array that was placed beneath a zigzag electrode with a small gap [66]. It relied on the piezoelectric potential created in a nanowire once subject to elastic straining, which drove the flow of charge carriers. The zigzag electrode acted as an array of parallel integrated tips for simultaneously collecting and outputting electricity from all of the active nanowires. In this design, the non-uniform heights and random distribution of the nanowires on the substrate, however, might prevent a large fraction of nanowires from contributing to the energy conversion process; a bottleneck in the application of nanogenerators is the output power. The output current of the nanogenerator is a sum of those contributed by all of the active nanowires, while the ultimate output voltage is determined by individual nanowires. The gap between the zigzag electrode and the nanowire arrays should be large enough to allow the nanowires to be freely deflected, but small enough to ensure an intimate contact between the nanowires and the electrode, which presents strict requirements for the packaging technology [87].

As an alternative, a novel approach that is composed of integrated, paired nanobrushes made of metal-coated ZnO nanotip arrays and bare ZnO nanowire arrays was demonstrated [88]. The overall structure is illustrated in Fig. 10a. Each layer of the nanogenerator has two terminals and is insulated from adjacent layers by an insulation layer embedded in the substrate. The nanotip and nanowire arrays were rationally synthesized on the two surfaces of a common substrate using the chemical method previously described, as shown in Figs. 10b,c. At a low growth temperature and long growth time, nanowires were formed, while at a relatively high growth temperature and short growth time, nanotips were grown [13]. For the aligned array, all of the nanowires have their positive *c*-axis pointing upwards, which means that the (0001) surface is at the growth front. This results in the alignment of dipoles and thus summation of the piezoelectric effect of all the nanowires, raising the output power (dramatically, etc.). The density of the ZnO nanowires and nanotips plays a critical role in the current-generating process. If it is too high, when the nanowire is bent by the nanotip, the nanowire would probably touch an adjacent nanowire, which would result in charge leakage and undermine the charge-accumulating process. This would in the end decrease the voltage output of the nanogenerator. If the density is too low, then the output power density of the nanogenerator would be rather limited. The operation of the nanogenerators relied on mechanical deflection of the nanowires but not the resonance of the nanowires. This largely expanded the application of the nanogenerators from the low-frequency domain (hertz range) to a relatively high-frequency domain (megahertz range).

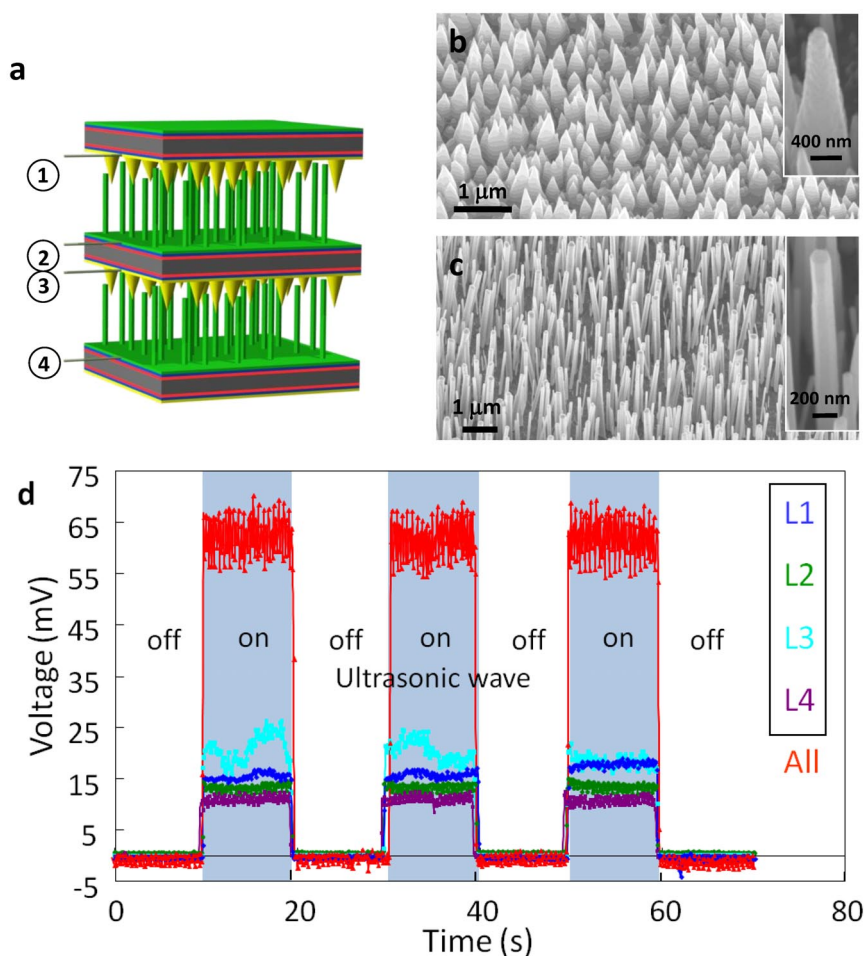


Fig. 10 (a) Structural design of the three-dimensional direct-current nanogenerator. SEM image of (b) ZnO nanotip and (c) nanowire arrays on two surfaces of a common substrate by rational wet chemical method. Insets show enlarged views. (d) Open-circuit voltage output measured from the four-layer integrated nanogenerator. The regions where the ultrasonic wave was on and off are indicated. The surface area of the nanogenerator was 6 mm² [88].

As the nanogenerator was subjected to ultrasonic wave excitation in a water bath, the ultrasonic wave would cause vibrations of the substrate and/or vibrations of the ZnO nanowires, resulting in relative bending/deflection of the nanowires as enforced by the Au-coated nanotips since the nanotips were significantly thicker and stiffer than the nanowires. Regardless of the bending direction, the currents generated by all of them add up as determined by the Schottky barrier and the uniaxial growth of the nanowires. Thousands to millions of nanowires contributed to the electric output in a random phase. Although each nanowire produces electric pulses only, the statistical average of the entire ensemble is considered to be in a steady state with continuous and constant output, as long as the ultrasonic wave is on.

The layer-by-layer integrated nanogenerators showed enhanced output current and voltage. By connecting two individual layers of nanogenerators in parallel/series, the output current/voltage was a sum of the two nanogenerators. When in an anti-parallel/anti-series connection, the output current/voltage was the difference of the two individual nanogenerators. Furthermore, as shown in Fig. 10c, four

individual layers of nanogenerators, L1, L2, L3, and L4 with 11, 14, 16, and 20 mV open-circuit output voltages, respectively, were connected in series, resulting in a total output voltage of ~62 mV and a maximum power output of 6.5 nW for a surface area of 6 mm². The power density was calculated to be as high as 0.11 μW/cm². The layer-by-layer assembly provides a feasible technology for building three-dimensional nanogenerators for applications where force or pressure variations are present, such as in the insole of shoes, under aircraft skins, or near the engine or tire of automobiles.

Multilayered alternating-current nanogenerator

Alternating-current nanogenerators were fabricated by vertically aligned ZnO nanowire arrays, in which all of the nanowires were connected in parallel, and each and every nanowire was working as a charge pump, independent from each other. The schematic representation of the structure is illustrated in Fig. 11a. Vertical ZnO nanowires were first grown on a Au-coated flat surface, forming Ohmic contact with the bottom Au electrode. A layer of PMMA was spin-coated onto the nanowires to wrap them to enhance their mechanical robustness and ensure insulation between the substrate and the top electrode. Subsequently, oxygen plasma etching was performed to expose the tips on the nanowires. A piece of Si wafer coated with a 300-nm-thick Pt film was then placed in direct contact with the nanowire tips as the top electrode and carefully packaged, creating a Schottky contact at the interface. Measurement was carried out in a Faraday cage, using a linear motor stimulator to generate the mechanical strain at an impact speed of 0.1 m/s. Typical *I*-*V* characteristics showed a rectification ratio of ~1000 at a bias voltage of 0.4 V.

Again, the crystallographic alignment of the nanowires led to the summation of piezoelectric charges in response to the external stress. When the negative piezoelectric potential is at the bottom Ohmic contact side and the positive potential is at the top Schottky contact side, the negative piezoelectric potential raises the local conduction band and the Fermi level in ZnO. Electrons will therefore flow from the nanowire bottom to the top electrode through the external circuit. The Schottky barrier at the top, however, obstructs the electrons from passing through the interface. These electrons are therefore blocked and accumulate around the tip of the nanowires, consequently elevating the Fermi level at the tip until the piezoelectric potential is fully “screened” and the Fermi levels of both sides reach a new equilibrium. During this process, the flow of electrons via the external circuit is detected as an electric pulse. As the external force is removed, the piezoelectric potential inside the nanowires diminishes. The electrons accumulated at the top then flow back via the external circuit (if leakage is negligible), creating an electric pulse in the opposite direction. Therefore, the piezoelectric potential acts as a “charging pump” that drives the electrons to flow. The same process occurs if the Schottky barrier is at the bottom or both sides of the nanowires. The key difference between alternating- and direct-current nanogenerators is that the mobile charges do not have to go across the interface through the ZnO nanowires for the alternating-current nanogenerator, while they have to for direct-current nanogenerator.

The output voltage and current could be greatly enhanced by linearly integrating a number of nanogenerators together [89,90]. Three nanogenerators with individual output voltages of 80, 90, and 96 mV, respectively, were connected in series, leading to an output voltage of 0.243 V (Fig. 11c). Likewise, the output current densities could be increased by connecting a number of nanogenerators in parallel. Theoretical calculations have shown that, within the linear elastic regime, the output voltage of a single nanowire is linearly proportional to the magnitude of its deformation. As we increase the pressing force acting on the nanowires, their deformation becomes larger, and the output voltage will linearly scale up. It must be noted that a large fraction of the applied stress was consumed in overcoming the elasticity of the packaging material (1–2 mm in thickness) around the nanogenerator. The magnitude of the output voltage also depended on the straining rate. The output signals of the nanogenerators were stable over a long period of time.

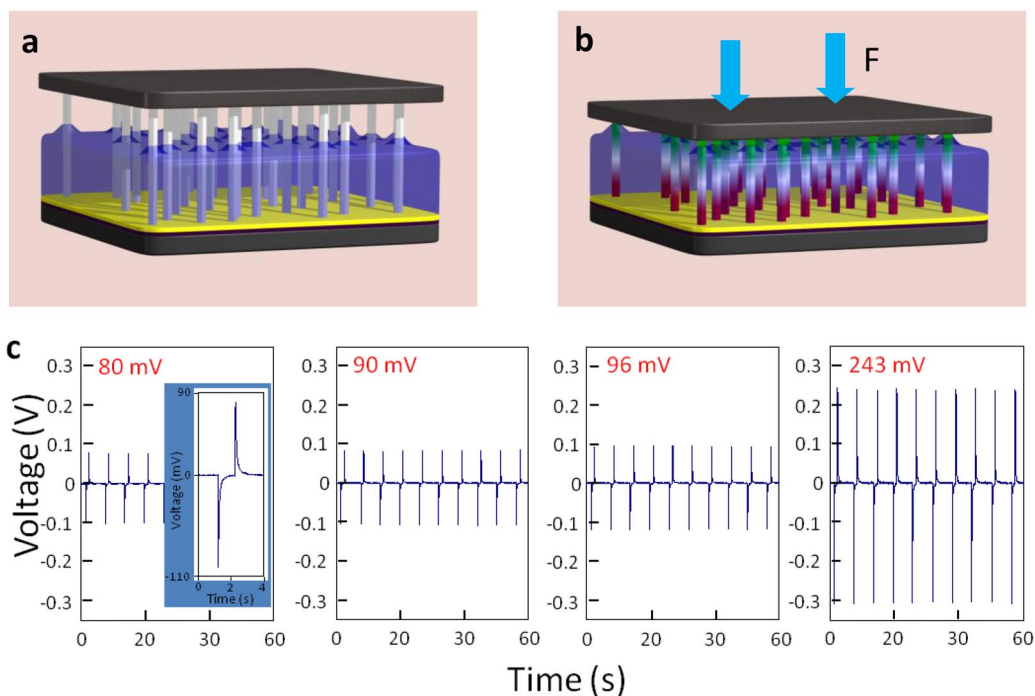


Fig. 11 (a) Structural design of one layer of alternating-current nanogenerator, and (b) the piezoelectric potential distribution along the nanowires when a uniaxial stress is applied at the top electrode. (c) Enhancing the output voltage of the nanogenerators by integrating them in series. Inset in the left panel is an enlarged view of a single electrical pulse [89].

It is widely known that ZnO has intrinsic *n*-type surface conductivity, which comes from the oxygen vacancies and zinc interstitial atoms. The piezoelectric potential may be partially screened by the carriers, which places fundamental limitations on the output voltage and thus output power of the nanogenerators [91]. As an alternative, alternating-current nanogenerators fabricated using the PZT nanowire arrays overcome this technical barrier owing to their insulating properties and a piezoelectric coefficient higher than ZnO. Assuming that (1) the elastic modulus of the nanowire is isotropic and the piezoelectric efficient is anisotropic; (2) the nanowire is under pure axial compression and free of shear strain; and (3) the piezoelectric domains are all perfectly aligned, finite element calculation has been carried out to estimate the piezo-potential. Based on a free-standing cantilever model, the result showed that, as shown in Fig. 12a, for a tetragonal PZT nanowire growing along [001] direction with a 500 nm diameter and 5 μm length, a uniaxial force of 2.5 μN could generate a piezoelectric potential (piezo-potential) of ~ 1 V.

To utilize this high piezo-potential, nanogenerators were fabricated based on PZT nanowire arrays grown on conductive Nb-doped STO substrates following the schematic shown in Fig. 12a. A piece of Si wafer coated with 50 nm Ti and 300 nm Pt was then packaged on top of the nanowire arrays as electrode. Three-dimensional integration of the nanogenerators was accomplished by stacking multiple layers of the described structure, and the entire structure was packaged with soft polymer to enhance robustness and isolate moisture erosion to the PZT nanowires. In the as-grown PZT nanowires, the dipole moments resulting from the position shift of the $\text{Ti}^{4+}/\text{Zr}^{4+}$ ions could take six possible orientations along $\langle 001 \rangle$, so electrical poling was required to align the piezoelectric dipoles in all of the nanowires, which was done by applying an external electric field of 100 KV/cm in a dielectric fluid. As a result, the dipole moments were forced to align normal to the substrate [92]. When the PZT nanowires

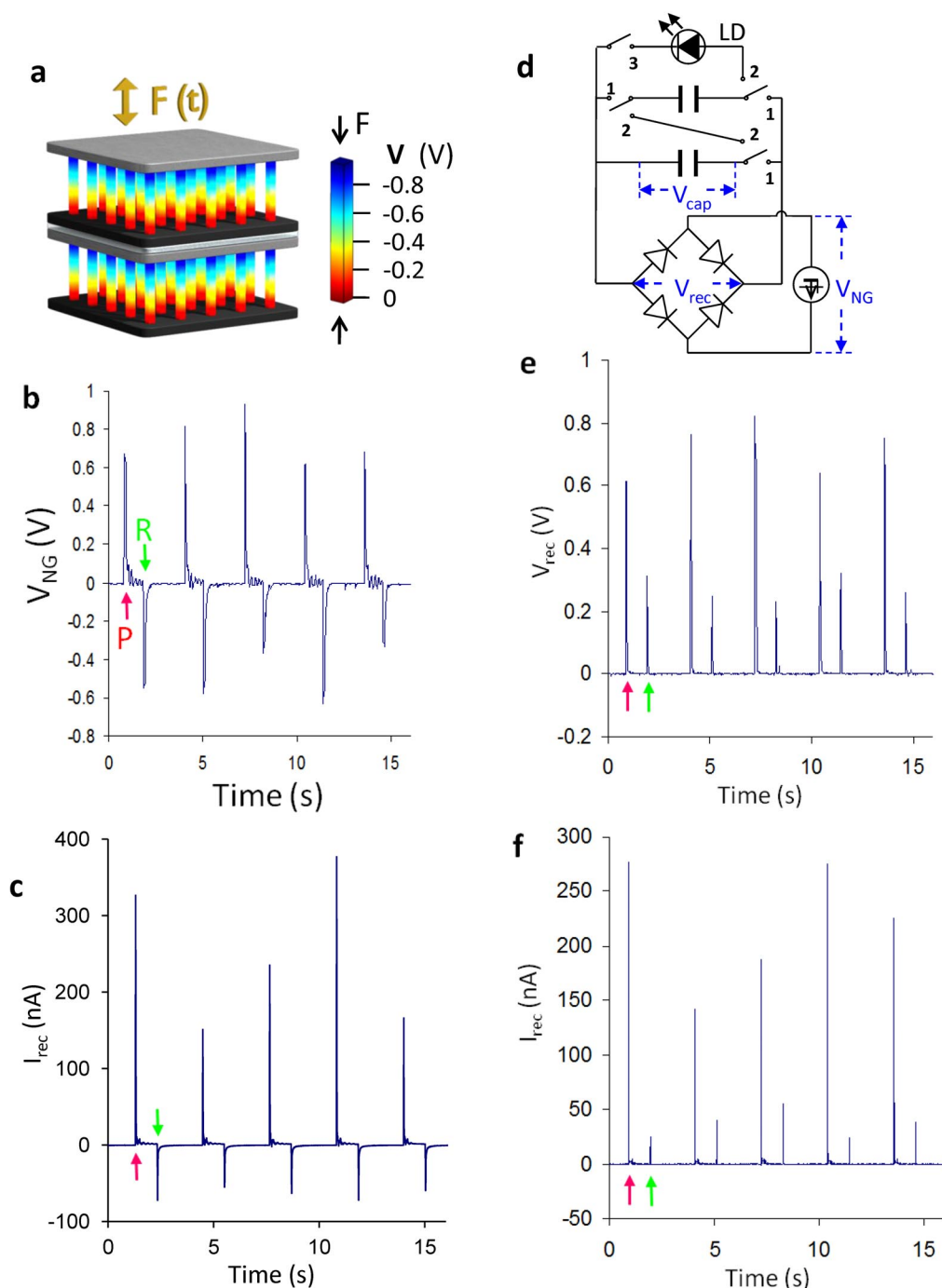


Fig. 12 (a) Schematic representation of the multilayered alternating current nanogenerator, and finite element calculation of the piezoelectric potential distribution (~ 1 V) in a PZT nanowire ($d_{33} = 1.52 \times 10^{-10}$ C/N). (b) Open-circuit voltage and (c) short-circuit current of a seven-layer integrated nanogenerator before rectification, where the electrical outputs when the nanogenerator was stressed and released are indicated with red and green arrowheads, respectively. (d) Design diagram of the rectifying circuit and charge storage devices, in which the measured voltages are labeled. (e) Open-circuit voltage and (f) short-circuit current of a seven-layer integrated nanogenerator after rectification [34].

are subject to a uniaxial compressive force, a piezoelectric field is created inside the nanowires, which produces a transient flow of the free electrons in the external load to screen the piezo-potential. When the force is removed, the piezo-potential diminishes, and the accumulated electrons are released. A dynamic stress drives the electrons in the external circuit to flow back and forth, resulting in an alternating output. Shown in Figs. 12b,c are the output voltage and current profile from a seven-layer integrated nanogenerator under a periodic mechanical pressing (P) and releasing (R). The output voltage is lower than the calculated result, owing to the following reasons. First, the height of the nanowires is non-uniform, and only a few percent of the nanowires are actively generating electricity. Second, the nanowires are not perfectly vertically aligned. So when the nanowires are under compression, shear strain is inevitable. Third, the remnant polarization after the electric field poling is relatively low. This could be improved by infiltration of insulating polymers into the spacing of the nanowires, which enables higher poling electric field.

Self-powered devices using nanogenerators

Building self-powered nanosystems is a future direction of nanotechnology. A nanosystem is a fully integrated system composed of nanodevices, functional components, and a power source. As shown in an inset in Fig. 13a, a vertical nanowire array nanogenerator was connected to a ZnO nanowire-based pH sensor. They were connected in series to form a loop. The voltage across the nanosensor was monitored by a voltmeter [93]. The pH sensor was coated with a 10 nm Si_3N_4 layer, and the testing was carried out within 1 h so that the etching effect to the ZnO nanowire from the solution was negligible. The Si_3N_4 layer was thin enough for the electrostatic interaction between the surface adsorbed charges and the carriers in the nanowire. By powering the pH sensor using a vertical array nanogenerator with an output voltage of ~ 40 mV, a clear sensitivity to local pH change was observed (Fig. 13a). When the buffer solution was basic, the surface of the nanosensor was dominated by $-\text{O}^-$ groups. Those negatively charged groups resulted in depletion regions at the surface of the *n*-type ZnO nanowire, which increased the resistance of the ZnO nanowire. Thus, the voltage drop on the ZnO nanowire was relatively high. As the buffer solution was changed from basic to acidic, the functional groups adsorbed on the surface of the nanosensor were gradually changed from $-\text{O}^-$ to $-\text{OH}_2^+$ groups. Therefore, the depletion regions at the ZnO nanowire surface diminished, which would lower the resistance of the ZnO nanowire. As we changed the pH value of the testing buffer solution from 10.01, 9.18, 7.01, 6.86, then to 4.01, the voltage drop on the pH sensor changed accordingly. A similar working principle also applies to other sensors, such as UV sensors. Similarly, by using a variable resistor, the voltage across the resistor was sensitive to the magnitude of its resistance and the result fits well to the linear circuit theory (Fig. 13b).

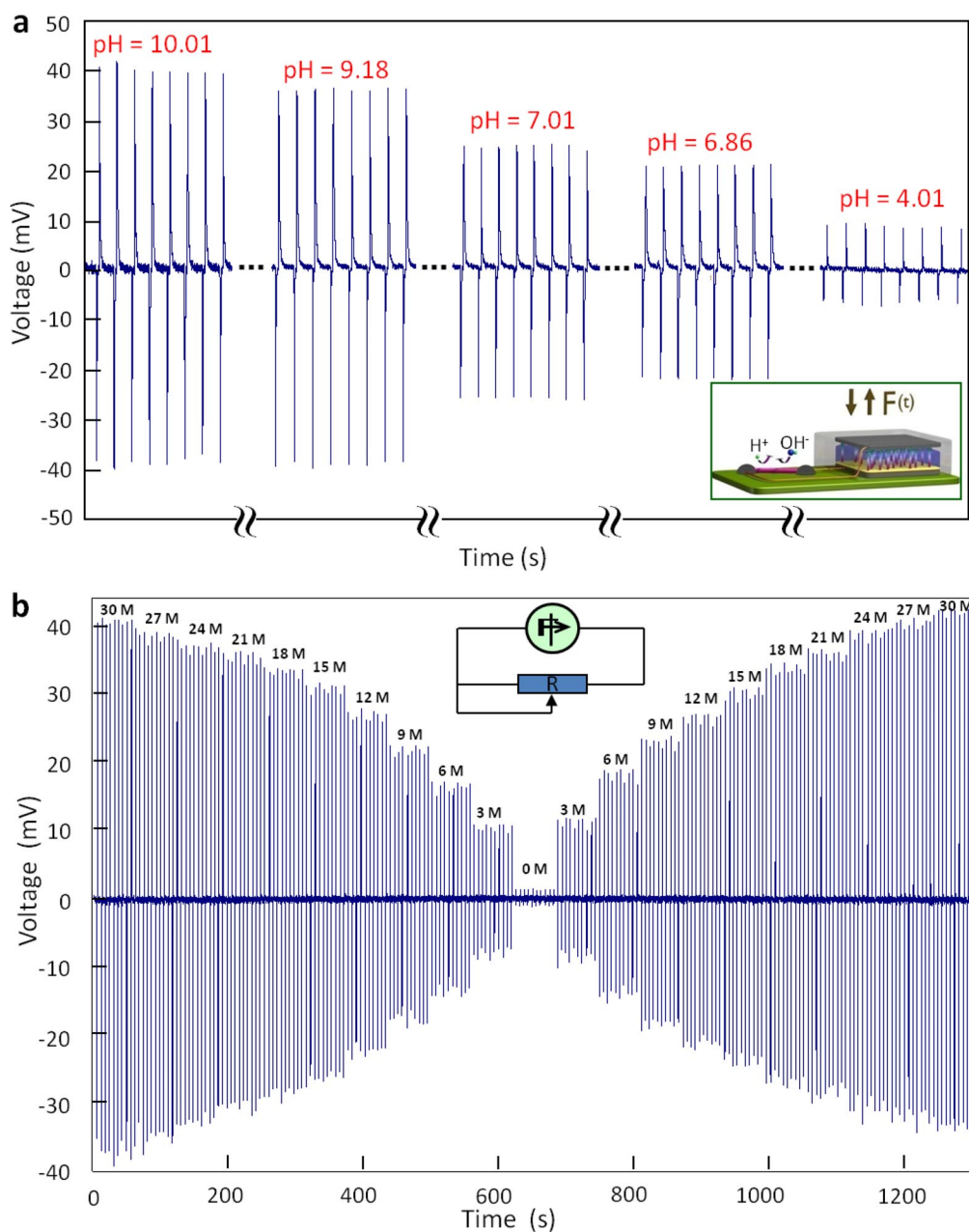


Fig. 13 (a) Voltage drop across a single ZnO nanowire-based pH sensor powered by a nanogenerator with an output voltage of 40 mV, showing a stepwise dropping of the voltage across the nanosensor as a function of its local pH value. The inset is schematic representation of the nanowire-based nanopower–nanodevice systems. (b) When gradually changing the amount of load resistance (from 0 to 30 M Ω), the magnitude of the voltage drop across the resistor changes accordingly. The voltage on the resistor is $V = V_0 R / (R + r)$, where V_0 is the open-circuit voltage of the nanogenerator, r is its inner resistance, and R is the resistance of the resistor [89].

Charge rectification and accumulation for powering microelectronic devices

Although the output voltage of nanogenerators has been steadily increased and a single nanowire-based pH sensor has been powered, the output power of the nanogenerators alone was still too small to power any conventional electronic components, such as LDs. Using a rectifying circuit, the output electrical energy of the nanogenerator was stored with capacitors and later used to light up a commercial LD. This is a pivotal step in developing sustainable energy technology for micro-/nanosystems.

To fully utilize the electrical energy harvested by the nanogenerator in one full cycle of mechanical deformation from both pressing and releasing, a current rectification and energy storage system was implemented using a commercial full-wave bridge rectifier composed of four diodes (Fig. 12d), each of which had a threshold voltage of 0.3–0.4 V as could be determined from their I - V curves. The voltage and current outputs of the nanogenerator after rectification are shown in Fig. 12e,f, clearly demonstrating full-wave rectification. Next, the generated charge pulses were stored consecutively by connecting eight 22 μ F capacitors in parallel, as shown in Fig. 12d with the switches set at position “1”.

The entire charging process was recorded by monitoring the voltage across a capacitor as presented in Fig. 14a. A step increase in the stored energy can be clearly seen with each cycle of the energy conversion process, as indicated by arrowheads in Fig. 14b. As the charging process continued, the voltage of the capacitor was saturated at \sim 0.42 V, which was lower than the peak output voltage of the nanogenerator and possibly caused by a voltage drop consumed at the rectifying diodes and/or the leakage of the capacitors, especially when the capacitor voltage was high. Then, by connecting the eight charged capacitors in series by adjusting the switches to position “2”, the total output voltage reached $V_{\text{tot}} = 0.42 \times 8 = 3.36$ V. When the switch “3” was turned on, the voltage drop across a capacitor dropped from \sim 0.42 to \sim 0.35 V after the discharge process (Fig. 14c, black curve). This means that \sim 16.7 % of the stored charges was effectively used to drive the LD. It is suggested that such a discharge behavior took place when the charges stored in the capacitor were insufficient to light the LD although the remaining voltage was enough to overcome the LD threshold but the current was limited. The remaining charges were still stored in the capacitor and blocked by the threshold operating voltage of the LD. The output power was derived from the discharge curve following $nCV_{\text{cap}}dV_{\text{cap}}/dt$, with n = number of capacitors in series. The fluctuation in power curve is due to differentiations of the noise in the V_{cap} curve. By utilizing this voltage amplification technique, a commercial LD (emission wavelength 650 nm, operation power 0.1–6 mW, turn-on voltage of \sim 1.5 V) was powered by a fast discharge of the stored charges, as shown in Fig. 14d. The next round of charging the capacitors would start at a base voltage of 0.35 V rather than 0 V, thus the following charging cycle should take a lot less time.

The power generated by such a small nanogenerator cannot drive the continuous operation of an LD. However, an accumulation of charges generated over a period of time is sufficient to drive the LD for a fraction of a second. This can be of practical use for devices that have standby and active modes, such as glucose sensors and blood pressure sensors for health monitoring, or even personal electronics such as Bluetooth[®] transmitters (driving power \sim 5 mW; data transmission rate \sim 500 Kbits/s; power consumption 10 nW/bit) that are only required to be in active mode periodically. The excess energy generated/harvested while the device is in standby mode is likely sufficient to drive the device when it is in active mode.

In comparison to its thin film counterparts, PZT nanowires have several noteworthy merits. First, single-crystal PZT thin films are fabricated at high temperatures using costly chemical vapor deposition [94], whereas facile growth of high-crystallinity PZT nanowires by wet chemical methods enables low-cost, large-scale device fabrication and the possibility of being transferred onto flexible substrates [32]. Second, the nanowires are highly elastic and fatigue-resistant, allowing large degrees of mechanical deformation without fracturing [95]. This greatly enhances the energy conversion efficiencies owing to nonlinear mechanical properties. Third, the force/stress required to induce the mechanical deformation of the nanowires is rather small in comparison to that needed to deform a solid thin-film-based energy harvester, thus permitting nanowire-based generators to operate in scenarios where only small trigger-

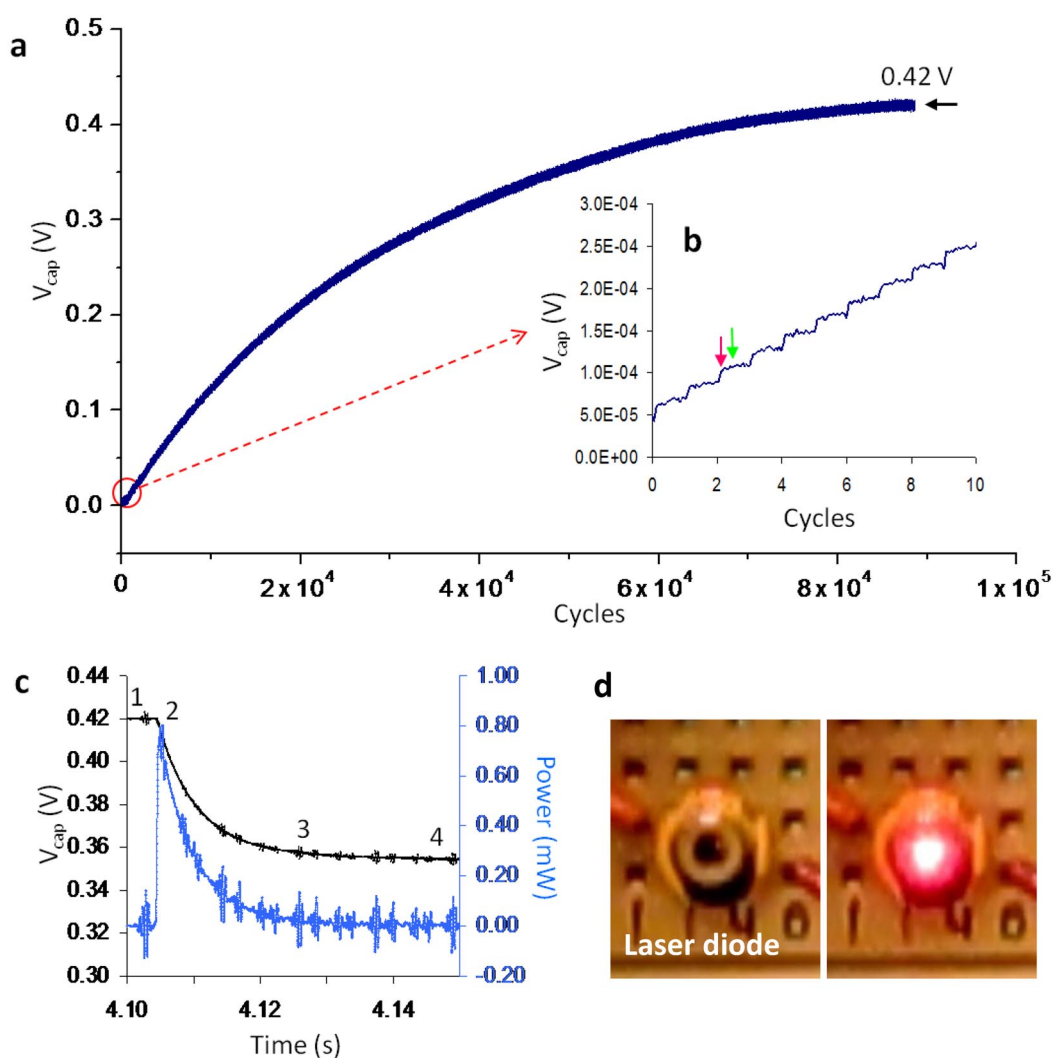


Fig. 14 (a) Voltage across a storage capacitor when being charged by an alternating-current nanogenerator with 0.7 V peak voltage. (b) An enlarged plot of the voltage curve in (a) at the very beginning of the charging process as indicated by a red circle. The step increases in capacitor voltage when the nanogenerator is compressed and released are indicated by red and green arrowheads, respectively. (c) Discharging voltage curve (black curve) across a single capacitor when it was connected in series together with seven other capacitors to an LD, and the corresponding output power to drive the LD (blue curve). V_{cap} saturates at 0.42 V (1~2). Then the capacitors discharged to light the LD, and the V_{cap} drops to 0.35 V (2~3) followed by a slow decay process (3~4). (d) Snapshots of the LD before and at the moment of being lit up using the stored charges [34].

ing forces are available [96]. Finally, the thin-film-based cantilever energy harvesters only work at their resonant frequencies [97]. In contrast, the generators based on nanowires do not require a specific driving frequency to operate, but can be driven by a wide range of random low-frequency mechanical agitations that are abundant in our daily life.

CONCLUSION

This review article presents the rational synthesis of ZnO and PZT nanowire arrays by wet chemical methods, and their applications in LEDs and piezoelectric nanogenerators. First, we have developed a unique technique for the low-temperature wet chemical growth of aligned ZnO and PZT nanowire arrays. Second, we have demonstrated the capability of controlling the spatial distribution of blue/near-UV LEDs composed of ordered arrays of *n*-ZnO nanowires on a *p*-GaN thin film substrate. The EL spectra have been decomposed to individual Gaussian subpeaks, which correspond to different electron hole recombination processes. The external quantum efficiency has been measured to be 2.5 % owing to a nanowire waveguiding effect. Third, we have utilized the as-grown ZnO and PZT nanowire arrays to fabricate the prototype piezoelectric nanogenerators that convert mechanical energy into direct- or alternating-current outputs. These nanogenerators have been used to power nanosensors in self-powered nanosystems, and the alternating output has been rectified and accumulated in capacitors to finally light up personal microelectronics, such as LDs. We believe that oxide nanowires will continue to make profound impacts in the research field of energy sciences.

ACKNOWLEDGMENTS

This research was supported by NSF, DOE, and DARPA. We thank those authors and many of our collaborators who made contributions to the published data reviewed in the text here.

REFERENCES

1. E. Serrano, G. Rus, J. García-Martínez. *Renew. Sust. Energy Rev.* **13**, 2373 (2009).
2. M. Law, L. E. Greene, J. C. Johnson, R. Saykally, P. D. Yang. *Nat. Mater.* **4**, 455 (2005).
3. G. Wang, H. Wang, Y. Ling, Y. Tang, X. Yang, R. C. Fitzmorris, C. Wang, J. Z. Zhang, Y. Li. *Nano Lett.* **11**, 3026 (2011).
4. D. K. Kim, P. Muralidharan, H. W. Lee, R. Ruffo, Y. Yang, C. K. Chan, H. Peng, R. A. Huggins, Y. Cui. *Nano Lett.* **8**, 3948 (2008).
5. Z. L. Wang, J. H. Song. *Science* **312**, 242 (2006).
6. P. C. Chen, G. Z. Shen, Y. Shi, H. T. Chen, C. W. Zhou. *ACS Nano* **4**, 4403 (2010).
7. W. I. Park, G. C. Yi. *Adv. Mater.* **16**, 87 (2004).
8. [Anon]. *Phys. World* **21**, 36 (2008).
9. Y. W. Heo, D. P. Norton, L. C. Tien, Y. Kwon, B. S. Kang, F. Ren, S. J. Pearton, J. R. LaRoche. *Mater. Sci. Eng. R* **47**, 1 (2004).
10. Z. L. Wang. *Mater. Today* **10**, 20 (2007).
11. L. Vayssieres, K. Keis, S. E. Lindquist, A. Hagfeldt. *J. Phys. Chem. B* **105**, 3350 (2001).
12. L. Vayssieres. *Adv. Mater.* **15**, 464 (2003).
13. S. Xu, C. Lao, B. Weintraub, Z. L. Wang. *J. Mater. Res.* **23**, 2072 (2008).
14. S. Xu, Z. L. Wang. *Nano Res.* (2011). doi:10.1007/s12274-011-0160-7
15. S. Xu, N. Adiga, S. Ba, T. Dasgupta, C. F. J. Wu, Z. L. Wang. *ACS Nano* **3**, 1803 (2009).
16. X. Gao, X. Li, W. Yu. *J. Phys. Chem. B* **109**, 1155 (2005).
17. C. F. J. Wu, S. S. Mao, F. S. S. Ma. S. Ghosh (Eds.). *Statistical Design and Analysis of Industrial Experiments*, Marcel Dekker, New York, 279 (1990).
18. C. F. J. Wu, M. Hamada. *Experiments: Planning, Analysis, and Optimization*, John Wiley, New York (2009).
19. Y. Liang, C. Zhen, D. Zou, D. Xu. *J. Am. Chem. Soc.* **126**, 16338 (2004).
20. S. Xu, Y. Wei, M. Kirkham, J. Liu, W. Mai, D. Davidovic, R. L. Snyder, Z. L. Wang. *J. Am. Chem. Soc.* **130**, 14958 (2008).

21. S. Xu, Y. Ding, Y. G. Wei, H. Fang, Y. Shen, A. K. Sood, D. L. Polla, Z. L. Wang. *J. Am. Chem. Soc.* **131**, 6670 (2009).
22. Y. Qin, R. S. Yang, Z. L. Wang. *J. Phys. Chem. C* **112**, 18734 (2008).
23. J. F. Conley, L. Stecker, Y. Ono. *Appl. Phys. Lett.* **87**, 223114 (2005).
24. W. I. Park, C. H. Lee, J. H. Chae, D. H. Lee, G. C. Yi. *Small* **5**, 181 (2009).
25. O. Harnack, C. Pacholski, H. Weller, A. Yasuda, J. M. Wessels. *Nano Lett.* **3**, 1097 (2003).
26. S. Xu, Y. Shen, Y. Ding, Z. L. Wang. *Adv. Funct. Mater.* **20**, 1493 (2010).
27. X. Chen, S. Y. Xu, N. Yao, W. H. Xu, Y. Shi. *Appl. Phys. Lett.* **95**, 253113 (2009).
28. R. Guo, L. E. Cross, S. E. Park, B. Noheda, D. E. Cox, G. Shirane. *Phys. Rev. Lett.* **84**, 5423 (2000).
29. R. Ramesh, W. K. Chan, B. Wilkens, H. Gilchrist, T. Sands, J. M. Tarascon, V. G. Keramidas, D. K. Fork, J. Lee, A. Safari. *Appl. Phys. Lett.* **61**, 1537 (1992).
30. X. Chen, S. Xu, N. Yao, Y. Shi. *Nano Lett.* **10**, 2133 (2010).
31. A. I. Kingon, S. Srinivasan. *Nat. Mater.* **4**, 233 (2005).
32. Y. Qi, N. T. Jafferis, K. Lyons, C. M. Lee, H. Ahmad, M. C. McAlpine. *Nano Lett.* **10**, 524 (2010).
33. K. S. Hwang, B. H. Kim. *Mater. Chem. Phys.* **57**, 224 (1999).
34. S. Xu, B. J. Hansen, Z. L. Wang. *Nat. Commun.* **1**, 93 (2010).
35. A. Tsukazaki, A. Ohtomo, T. Onuma, M. Ohtani, T. Makino, M. Sumiya, K. Ohtani, S. F. Chichibu, S. Fuke, Y. Segawa, H. Ohno, H. Koinuma, M. Kawasaki. *Nat. Mater.* **4**, 42 (2005).
36. Y. I. Alivov, J. E. Van Nostrand, D. C. Look, M. V. Chukichev, B. M. Ataev. *Appl. Phys. Lett.* **83**, 2943 (2003).
37. S. Xu, C. Xu, Y. Liu, Y. Hu, R. Yang, Q. Yang, J. H. Ryou, H. J. Kim, Z. Lochner, S. Choi, R. Dupuis, Z. L. Wang. *Adv. Mater.* **22**, 4749 (2010).
38. D. C. Look, B. Claflin, Y. I. Alivov, S. J. Park. *Phys. Status Solidi A* **201**, 2203 (2004).
39. K. A. Bulashevich, I. Y. Evstratov, S. Y. Karpov. *Phys. Status Solidi A* **204**, 241 (2007).
40. I. E. Titkov, A. S. Zubrilov, L. A. Delimova, D. V. Mashovets, I. A. Liniichuk, I. V. Grekhov. *Semiconductor* **41**, 564 (2007).
41. I. E. Titkov, L. A. Delimova, A. S. Zubrilov, N. V. Seredova, I. A. Liniichuk, I. V. Grekhov. *J. Mod. Optic.* **56**, 653 (2009).
42. A. M. C. Ng, Y. Y. Xi, Y. F. Hsu, A. B. Djurisic, W. K. Chan, S. Gwo, H. L. Tam, K. W. Cheah, P. W. K. Fong, H. F. Lui, C. Surya. *Nanotechnology* **20**, 445201 (2009).
43. H. Y. Xu, Y. C. Liu, Y. X. Liu, C. S. Xu, C. L. Shao, R. Mu. *Appl. Phys. B* **80**, 871 (2005).
44. Y. I. Alivov, U. Ozgur, S. Dogan, C. Liu, Y. Moon, X. Gu, V. Avrutin, Y. Fu, H. Morkoc. *Solid State Electron.* **49**, 1693 (2005).
45. X. M. Zhang, M. Y. Lu, Y. Zhang, L. J. Chen, Z. L. Wang. *Adv. Mater.* **21**, 2767 (2009).
46. J. J. Cole, X. Wang, R. J. Knuesel, H. O. Jacobs. *Nano Lett.* **8**, 1477 (2008).
47. R. Guo, J. Nishimura, M. Matsumoto, M. Higashihata, D. Nakamura, T. Okada. *Appl. Phys. B* **94**, 33 (2009).
48. H. F. Liu, G. X. Hu, H. Gong, K. Y. Zang, S. J. Chua. *J. Vac. Sci. Technol. A* **26**, 1462 (2008).
49. C. Bayram, F. H. Teherani, D. J. Rogers, M. Razeghi. *Appl. Phys. Lett.* **93**, 081111 (2008).
50. H. W. Choi, C. W. Jeon, M. D. Dawson, P. R. Edwards, R. W. Martin, S. Tripathy. *J. Appl. Phys.* **93**, 5978 (2003).
51. I. Schnitzer, E. Yablonovitch, C. Caneau, T. J. Gmitter, A. Scherer. *Appl. Phys. Lett.* **63**, 2174 (1993).
52. H. Kim, K.-K. Kim, K.-K. Choi, H. Kim, J.-O. Song, J. Cho, K. H. Baik, C. Sone, Y. Park, T.-Y. Seong. *Appl. Phys. Lett.* **91**, 023510 (2007).
53. E. F. Schubert, J. K. Kim. *Science* **308**, 1274 (2005).
54. W. L. Barnes. *J. Lightwave Technol.* **17**, 2170 (1999).
55. T. N. Oder, K. H. Kim, J. Y. Lin, H. X. Jiang. *Appl. Phys. Lett.* **84**, 466 (2004).

56. J. Zhong, H. Chen, G. Saraf, Y. Lu, C. K. Choi, J. J. Song, D. M. Mackie, H. Shen. *Appl. Phys. Lett.* **90**, 203515 (2007).
57. S. J. An, J. H. Chae, G. C. Yi, G. H. Park. *Appl. Phys. Lett.* **92**, 121108 (2008).
58. K. S. Kim, S.-M. Kim, H. Jeong, M. S. Jeong, G. Y. Jung. *Adv. Funct. Mater.* **20**, 1076 (2010).
59. K. K. Kim, S. D. Lee, H. Kim, J. C. Park, S. N. Lee, Y. Park, S. J. Park, S. W. Kim. *Appl. Phys. Lett.* **94**, 071118 (2009).
60. E. Lai, W. Kim, P. Yang. *Nano Res.* **1**, 123 (2008).
61. H. Sekiguchi, K. Kato, J. Tanaka, A. Kikuchi, K. Kishino. *Phys. Status Solidi A* **205**, 1067 (2008).
62. S. H. Park, S. H. Kim, S. W. Han. *Nanotechnology* **18**, 055608 (2007).
63. B. Z. Tian, X. L. Zheng, T. J. Kempa, Y. Fang, N. F. Yu, G. H. Yu, J. L. Huang, C. M. Lieber. *Nature* **449**, 885 (2007).
64. Z. L. Wang. *Sci. Am.* **298**, 82 (2008).
65. C. F. Pan, H. Wu, C. Wang, B. Wang, L. Zhang, Z. D. Cheng, P. Hu, W. Pan, Z. Y. Zhou, X. Yang, J. Zhu. *Adv. Mater.* **20**, 1644 (2008).
66. X. D. Wang, J. H. Song, J. Liu, Z. L. Wang. *Science* **316**, 102 (2007).
67. M. Y. Choi, D. Choi, M. J. Jin, I. Kim, S. H. Kim, J. Y. Choi, S. Y. Lee, J. M. Kim, S. W. Kim. *Adv. Mater.* **21**, 2185 (2009).
68. Y. Lei, Z. Jiao, M. H. Wu, G. Wilde. *Adv. Eng. Mater.* **9**, 343 (2007).
69. R. S. Yang, Y. Qin, L. M. Dai, Z. L. Wang. *Nat. Nanotechnol.* **4**, 34 (2009).
70. W. S. Su, Y. F. Chen, C. L. Hsiao, L. W. Tu. *Appl. Phys. Lett.* **90**, 063110 (2007).
71. W. S. Su, Y. F. Chen, C. L. Hsiao, L. W. Tu. *Appl. Phys. Lett.* **90**, 179901 (2007).
72. C. T. Huang, J. H. Song, W. F. Lee, Y. Ding, Z. Y. Gao, Y. Hao, L. J. Chen, Z. L. Wang. *J. Am. Chem. Soc.* **132**, 4766 (2010).
73. C. T. Huang, J. H. Song, C. M. Tsai, W. F. Lee, D. H. Lien, Z. Y. Gao, Y. Hao, L. J. Chen, Z. L. Wang. *Adv. Mater.* **22**, 4008 (2010).
74. X. B. Wang, J. H. Song, F. Zhang, C. Y. He, Z. Hu, Z. L. Wang. *Adv. Mater.* **22**, 2155 (2010).
75. Y. F. Lin, J. Song, Y. Ding, S. Y. Lu, Z. L. Wang. *Adv. Mater.* **20**, 3127 (2008).
76. M. Y. Lu, J. H. Song, M. P. Lu, C. Y. Lee, L. J. Chen, Z. L. Wang. *ACS Nano* **3**, 357 (2009).
77. Y. Qi, M. C. McAlpine. *Energy Environ. Sci.* **3**, 1275 (2010).
78. X. Feng, B. D. Yang, Y. M. Liu, Y. Wang, C. Dagdeviren, Z. J. Liu, A. Carlson, J. Y. Li, Y. G. Huang, J. A. Rogers. *ACS Nano* **5**, 3326 (2011).
79. M. H. Lee, A. Javey. *Nature* **472**, 304 (2011).
80. Y. Qi, J. Kim, T. D. Nguyen, B. Lisko, P. K. Purohit, M. C. McAlpine. *Nano Lett.* **11**, 1331 (2011).
81. S. Y. Xu, Y. Shi. *J. Phys. D: Appl. Phys.* **42**, 085301 (2009).
82. Z. Y. Wang, J. Hu, A. P. Suryavanshi, K. Yum, M. F. Yu. *Nano Lett.* **7**, 2966 (2007).
83. T. Y. Ke, H. A. Chen, H. S. Sheu, J. W. Yeh, H. N. Lin, C. Y. Lee, H. T. Chiu. *J. Phys. Chem. C* **112**, 8827 (2008).
84. C. Chang, V. H. Tran, J. Wang, Y.-K. Fuh, L. Lin. *Nano Lett.* **10**, 726 (2010).
85. B. J. Hansen, Y. Liu, R. S. Yang, Z. L. Wang. *ACS Nano* **4**, 3647 (2010).
86. R. F. Service. *Science* **328**, 304 (2010).
87. Y. Qin, X. D. Wang, Z. L. Wang. *Nature* **451**, 809 (2008).
88. S. Xu, Y. G. Wei, J. Liu, R. Yang, Z. L. Wang. *Nano Lett.* **8**, 4027 (2008).
89. S. Xu, Y. Qin, C. Xu, Y. G. Wei, R. S. Yang, Z. L. Wang. *Nat. Nanotechnol.* **5**, 366 (2010).
90. A. F. Yu, H. Y. Li, H. Y. Tang, T. J. Liu, P. Jiang, Z. L. Wang. *Phys. Status Solidi R* **5**, 162 (2011).
91. Y. Gao, Z. L. Wang. *Nano Lett.* **9**, 1103 (2009).
92. B. P. Zhu, Q. F. Zhou, J. Shi, K. K. Shung, S. Irisawa, S. Takeuchi. *Appl. Phys. Lett.* **94**, 102901 (2009).
93. B. S. Kang, F. Ren, Y. W. Heo, L. C. Tien, D. P. Norton, S. J. Pearton. *Appl. Phys. Lett.* **86**, 112105 (2005).

94. C. M. Foster, G. R. Bai, R. Csencsits, J. Vetrone, R. Jammy, L. A. Wills, E. Carr, J. Amano. *J. Appl. Phys.* **81**, 2349 (1997).
95. Z. Y. Gao, Y. Ding, S. S. Lin, Y. Hao, Z. L. Wang. *Phys. Status Solidi R* **3**, 260 (2009).
96. R. Yang, Y. Qin, C. Li, G. Zhu, Z. L. Wang. *Nano Lett.* **9**, 1201 (2009).
97. Y. B. Jeon, R. Sood, J. H. Jeong, S. G. Kim. *Sens. Actuators, A* **122**, 16 (2005).